Supplementary Information (SI) for Energy & Environmental Science.
This journal is © The Royal Society of Chemistry 2026

Supporting Information

A High-Adaptability Ambient Energy Harvester Enhanced by the Canyon Effect for Smart Agriculture

Weilin Liao[a], Xiaosen Su[a], Huikang Li[a], Zijian Huang[d], Bingcheng Li[a], Jinsong Cai[a], Fei Fang[a,], Ke Zhang[b], Xudong Huang[b,*], Zhong Lin Wang[c,e*]*

a. Department of Engineering Mechanics, Tsinghua University, Beijing 100084, P. R. China

b. Department of Aeronautics and Astronautics, Tsinghua University, Beijing 100084, PR China

c. Beijing Key Laboratory of High-Entropy Energy Materials and Devices, Beijing Institute of Nanoenergy and Nanosystems, Chinese Academy of Sciences, Beijing, P. R. China

d. Key Laboratory of Bionic Engineering, Ministry of Education, Jilin University, Changchun 130000, P. R. China

e. Department of Materials Science and Engineering, Kyung Hee University, Yongin 17104, Republic of Korea

E-mail: fangf@mail.tsinghua.edu.cn, xdhuang@mail.tsinghua.edu.cn, zhong.wang@mse.gatech.edu

Table of Contents

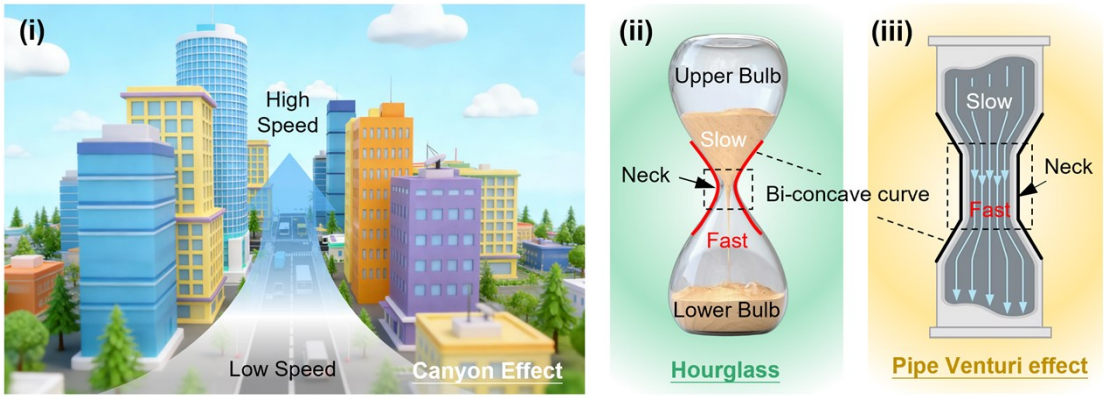

Fig. S1. The urban canyon effect, pipe Venturi effect, and sand acceleration phenomenon in an hourglass.

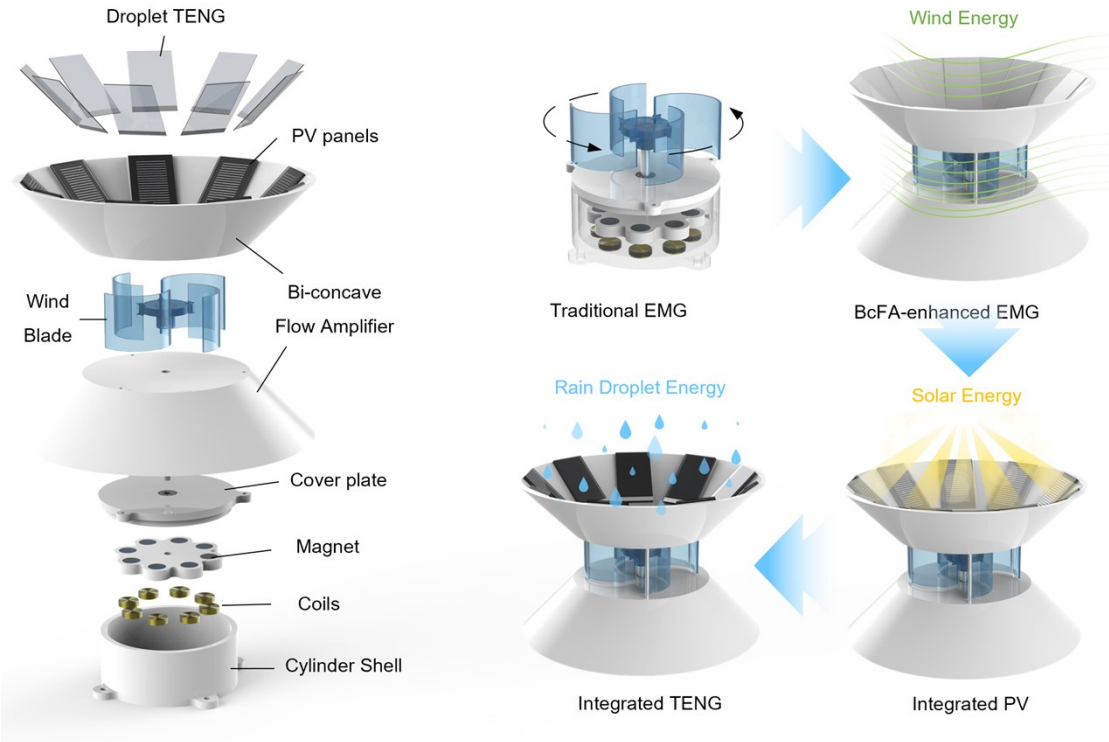

Fig. S2. Exploded view and module integration process of the WSR-EH.

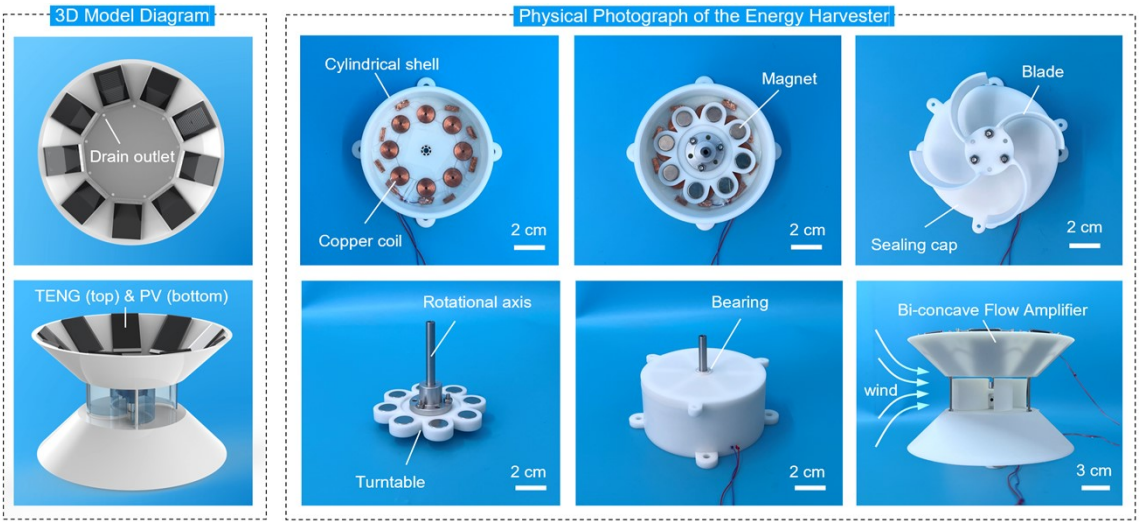

Fig. S3. 3D schematic diagram and prototype photos of WSR-EH.

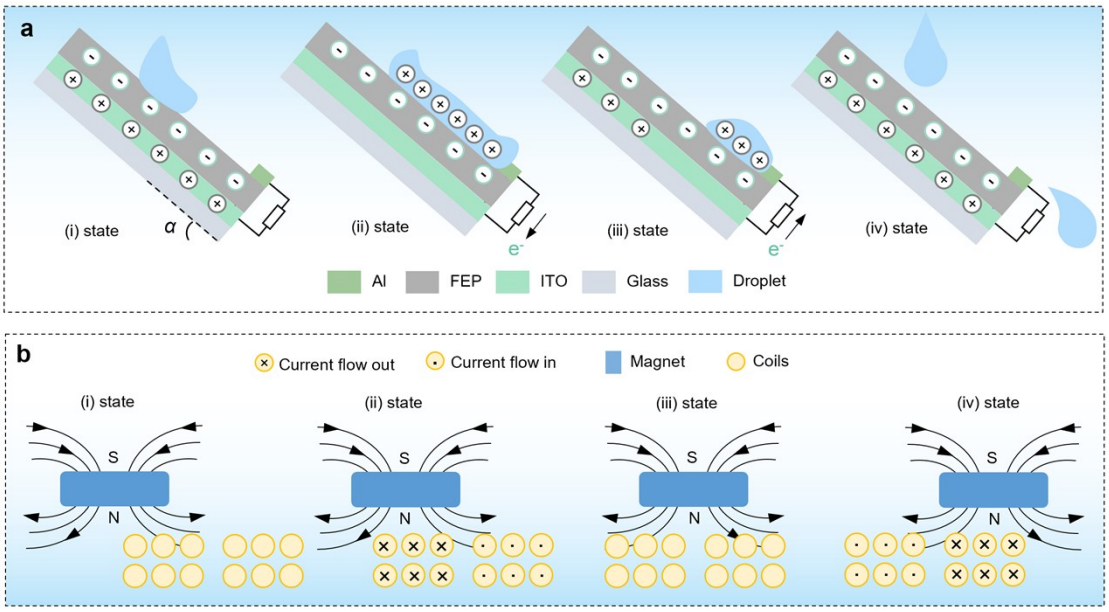

Fig. S4. Schematic diagram of power generation mechanisms. (a) Droplet TENG; (b) EMG.

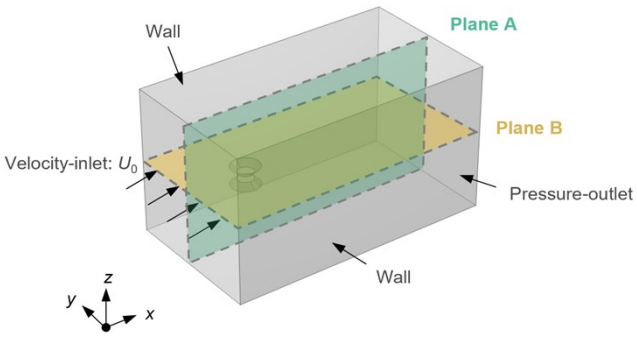

Fig. S5. Simulation model of BcFA.

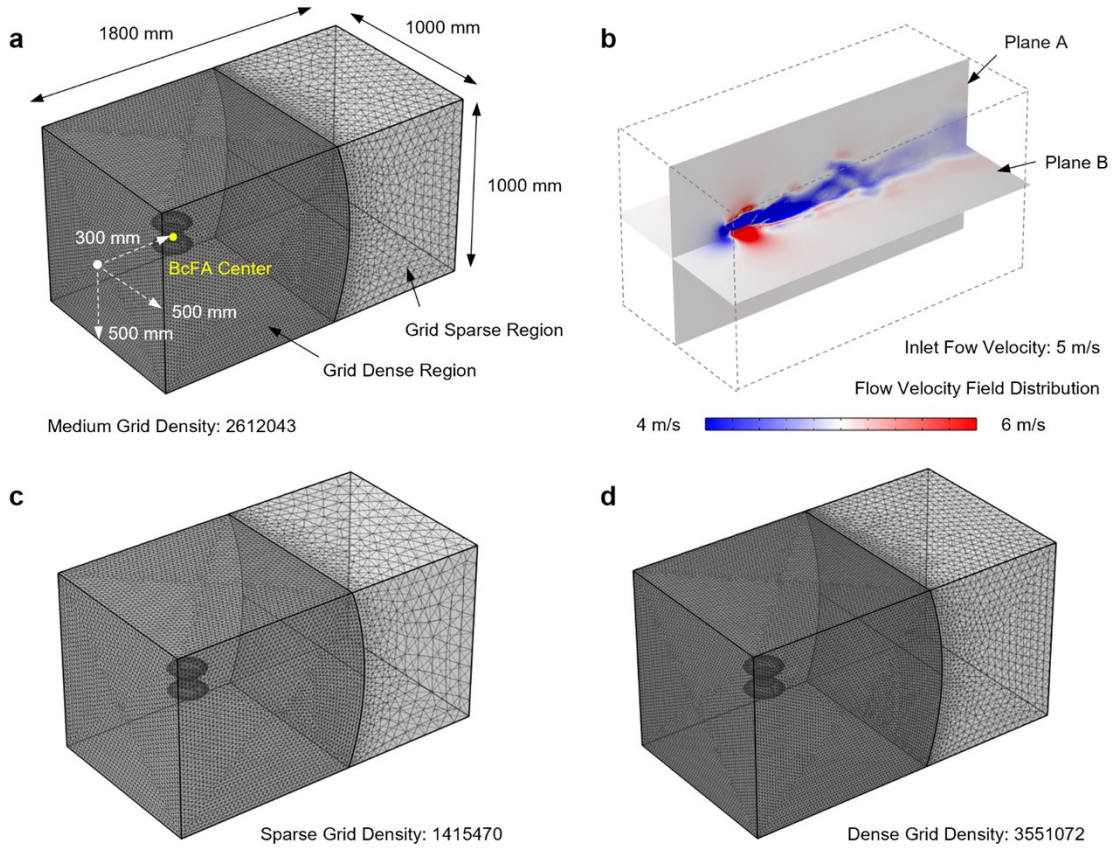

Fig. S6. Simulation mesh and dimensional information. (a) Medium grid model and size settings; (b) Flow velocity distributions in plane-A and plane-B from medium grid calculations; (c) Sparse grid; (d) Dense grid.

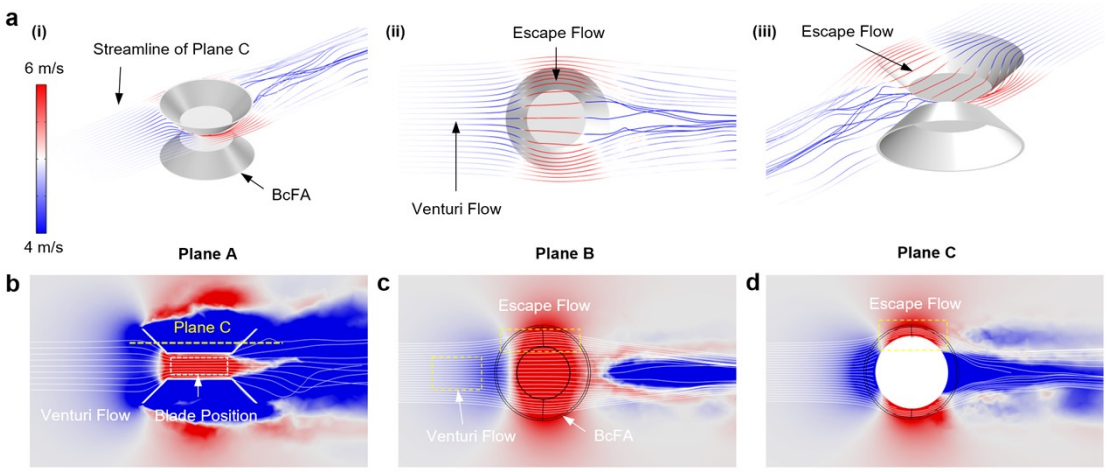

Fig. S7. Streamline distribution of BcFA. (a) Streamline distribution around the BcFA at an inlet velocity of 5 m/s; (b) Streamlines in plane-A; (c) Streamlines in plane-B; (d) Streamlines in plane-C.

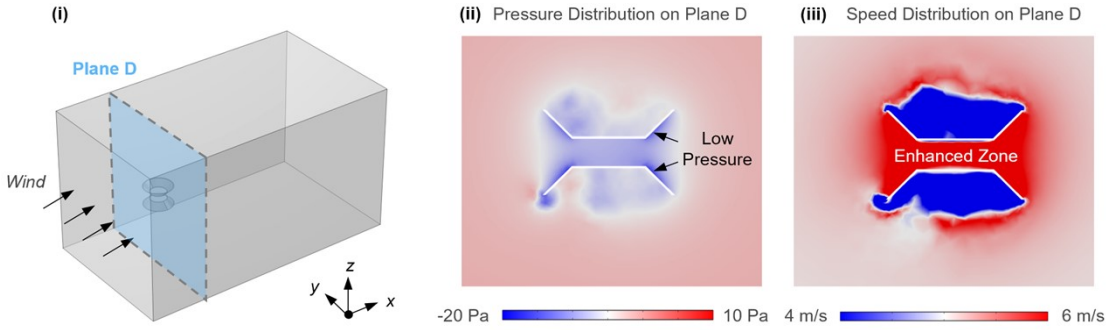

Fig. S8. Plane-D configuration of BcFA and its pressure and velocity distribution.

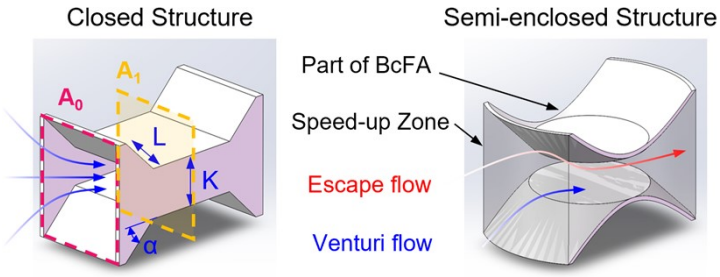

Fig. S9. Flow acceleration in different structures.

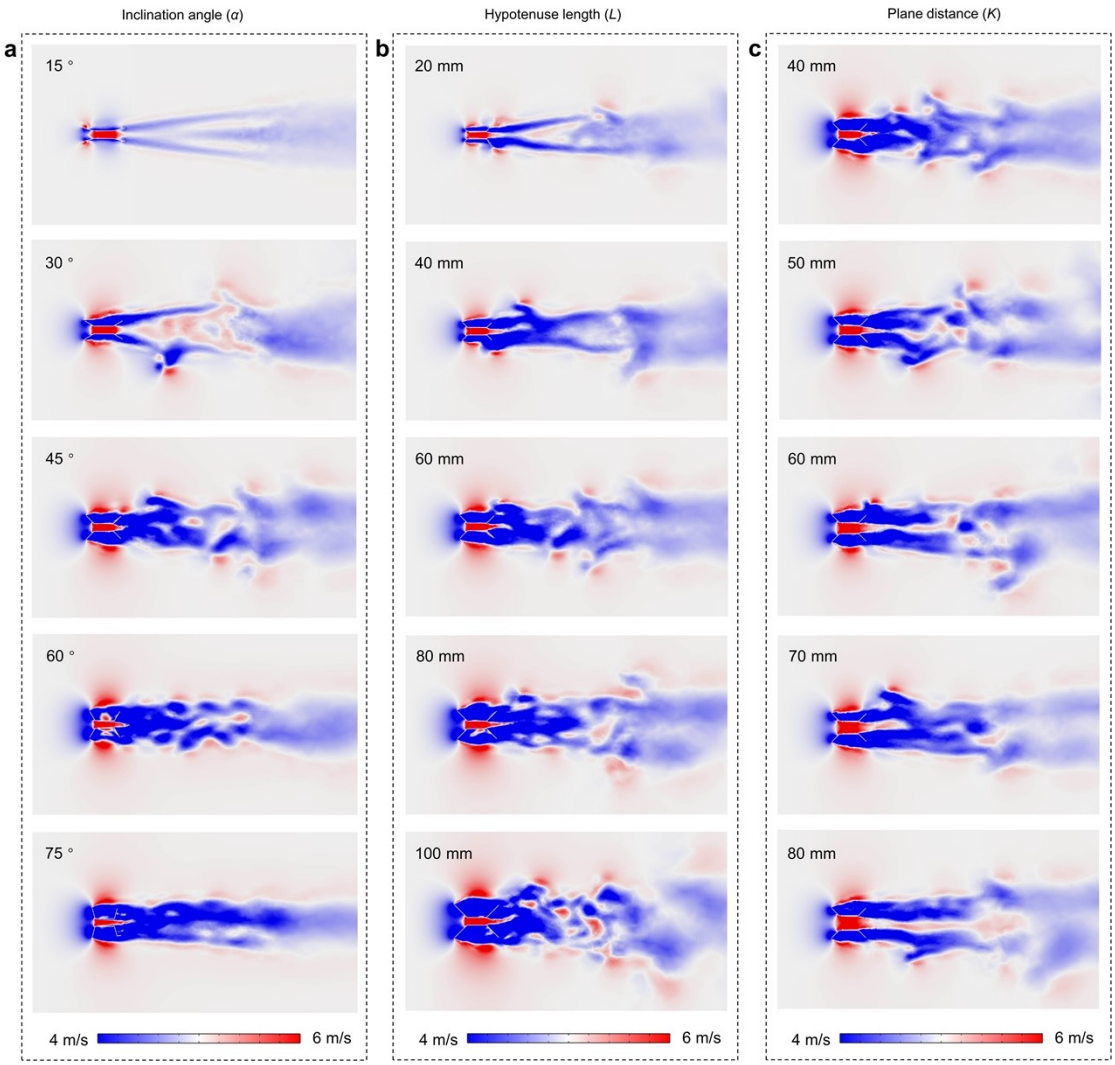

Fig. S10. Influence of BcFA structural parameters on the velocity field distribution in plane-A. (a) Effect of inclination angle; (b) Effect of hypotenuse length; (c) Effect of plane distance.

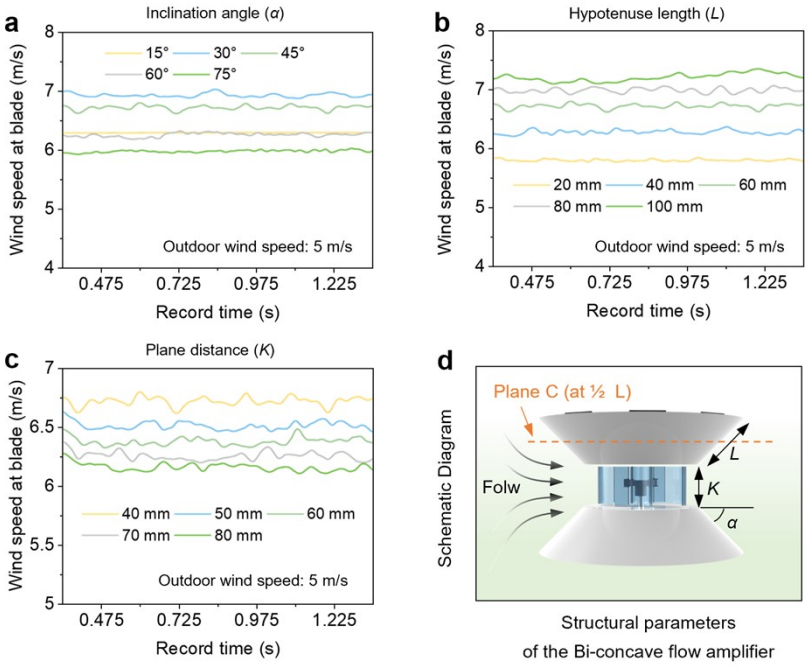

Fig. S11. Effect of structural parameters on flow velocity at the blade in BcFA. (a) Effect of inclination angle; (b) Effect of hypotenuse length; (c) Effect of plane distance; (d) Parameter settings diagram.

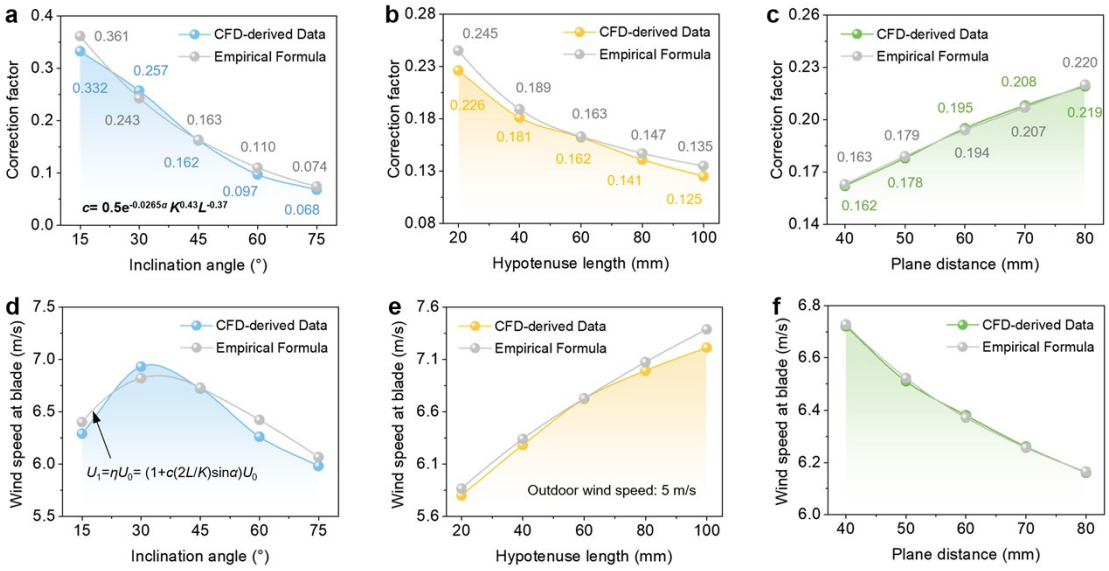

Fig. S12. Effect of structural parameters on factor *c* and average flow velocity of the blade. Effects of (a) inclination angle, (b) hypotenuse length, and (c) plane distance on correction factor *c*; Effects of (d) inclination angle, (e) hypotenuse length, and (f) plane distance on average flow velocity at the blade.

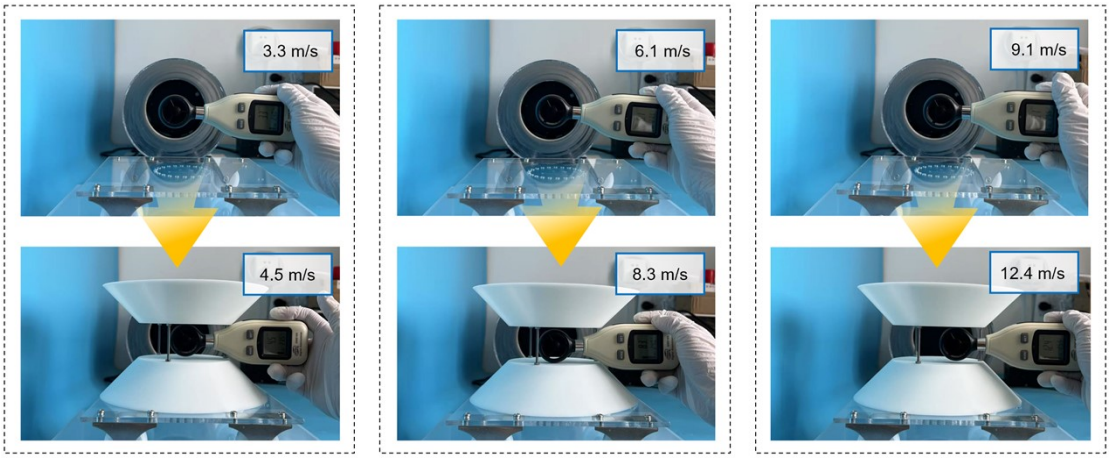

Fig. S13. Flow enhancement testing of BcFA at different wind speeds.

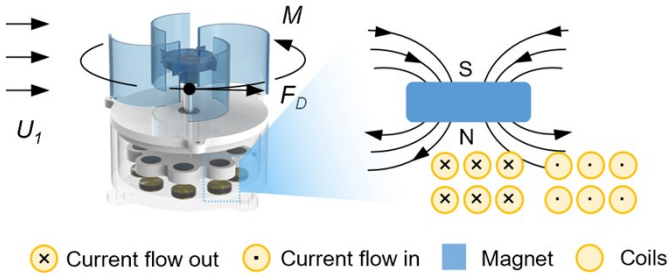

Fig. S14. Schematic diagram of an EMG driven by vertical-axis blades.

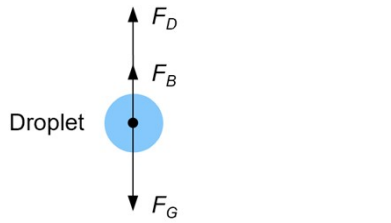

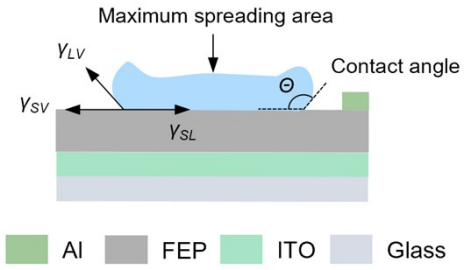

Fig. S15. Schematic diagram of raindrops falling and spreading.

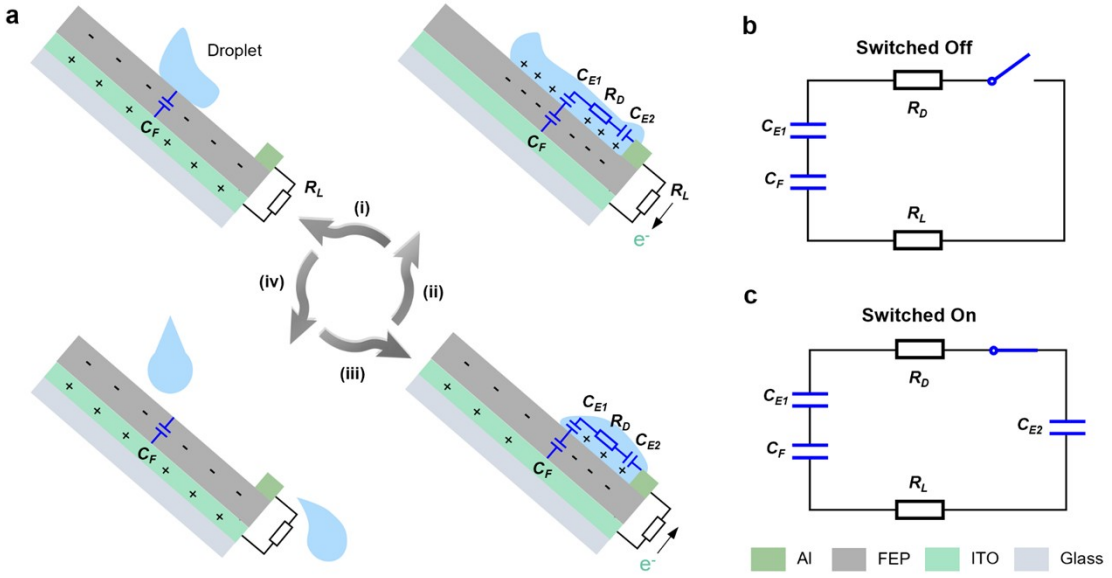

Fig. S16. Circuit model of droplet TENG. (a) TENG power generation mechanism; (b, c) Circuit schematic of TENG.

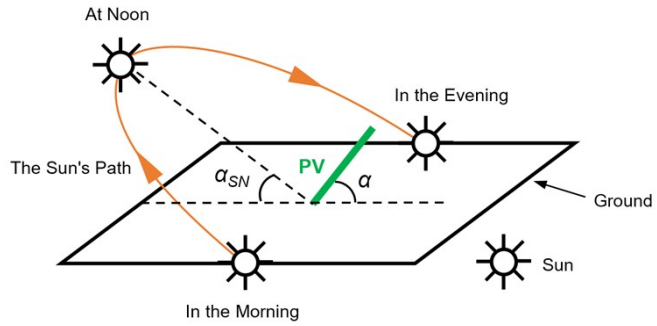

Fig. S17. Diagram of solar altitude angle and PV panel installation angle.

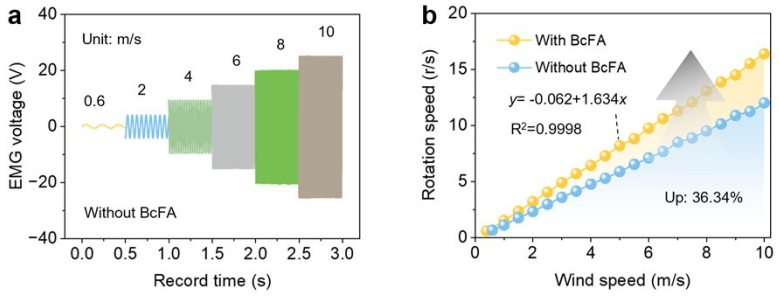

Fig. S18. EMG voltage and rotational speed without BcFA enhancement. (a) Voltage curves at different wind speeds; (b) Comparison of rotational speed between BcFA-enhanced and normal EMG states.

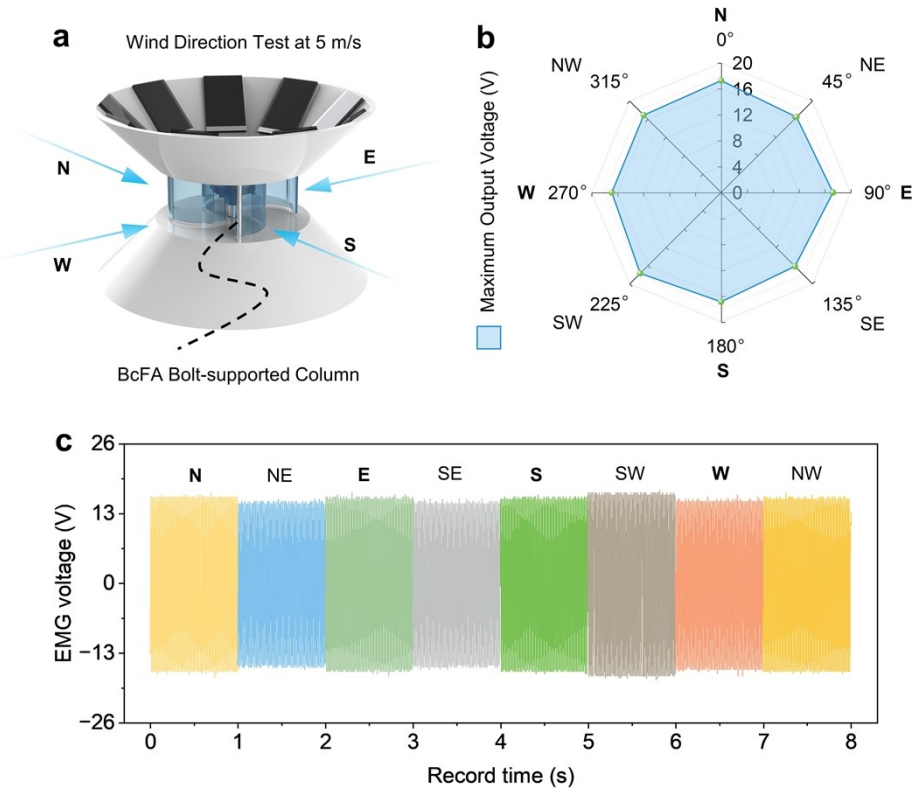

Fig. S19. The wind direction sensitivity of the EMG. (a) Wind direction diagram; (b) Peak EMG voltages under different wind directions; (c) EMG voltage curves under different wind directions.

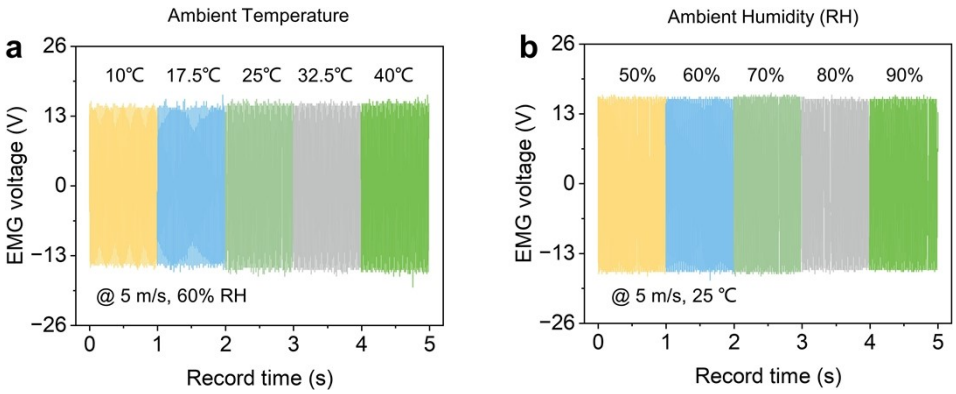

Fig. S20. Temperature and humidity dependency testing of EMG. (a) EMG voltage output at different temperatures; (b) EMG voltage output at different humidities.

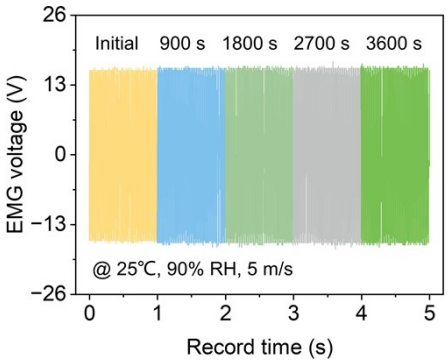

Fig. S21. EMG durability testing for 3600 seconds in a 90 % RH environment.

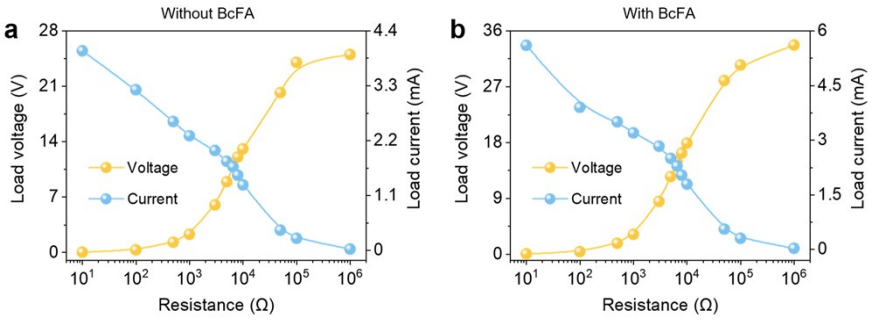

Fig. S22. Load current and voltage curves of EMG. (a) Voltage and current curves of EMG without BcFA enhancement; (b) Voltage and current curves of EMG with BcFA enhancement.

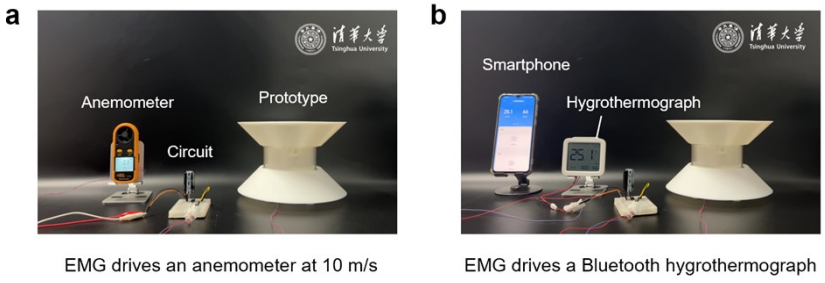

Fig. S23. EMG application demonstration. (a) Driving an anemometer via EMG; (b) Driving a Bluetooth thermo-hygrometer via EMG.

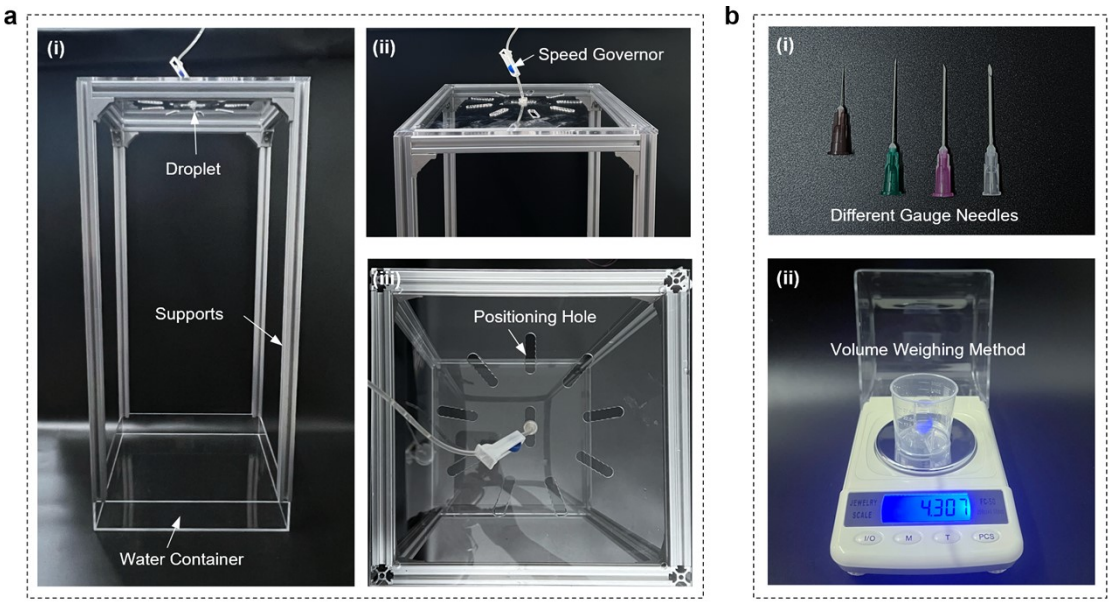

Fig. S24. Testing system and droplet volume adjustment strategy for the droplet TENG.

Fig. S25. Photographs of PVC-based TENG, PET-based TENG, and PTFE-based TENG under natural light.

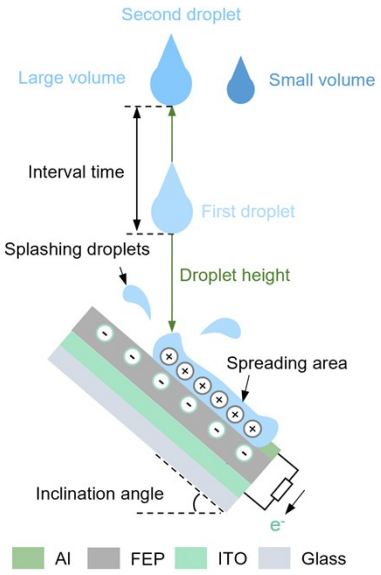

Fig. S26. Schematic diagram for droplet parameter settings.

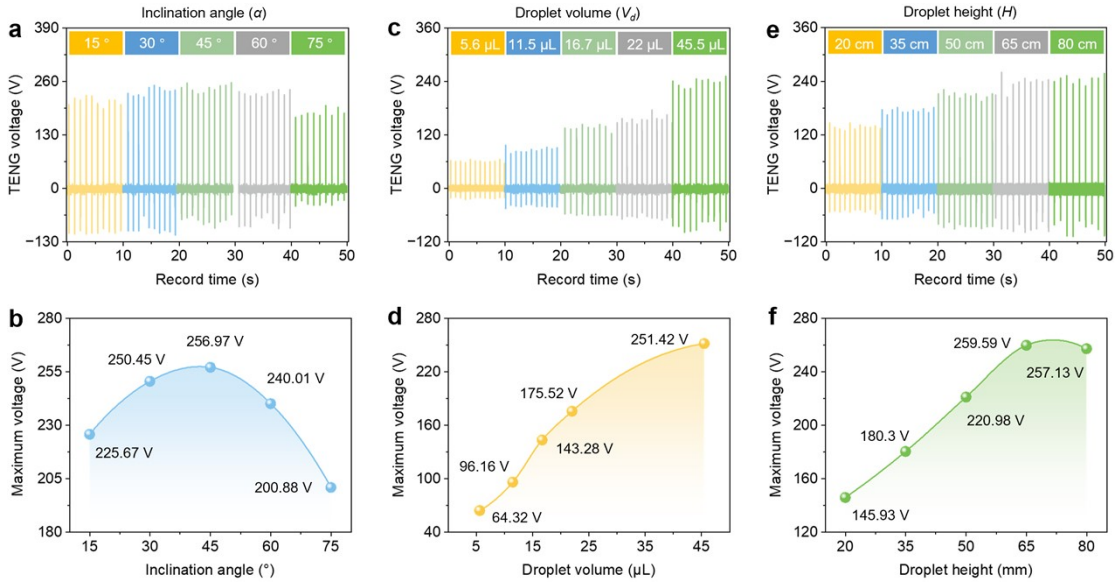

Fig. S27. Effect of droplet parameters on TENG voltage. (a) Voltage curves and (b) peak voltage at different inclination angles; (c) Voltage curves and (d) peak voltage at different droplet volumes; (e) Voltage curves and (f) peak voltage at different droplet heights.

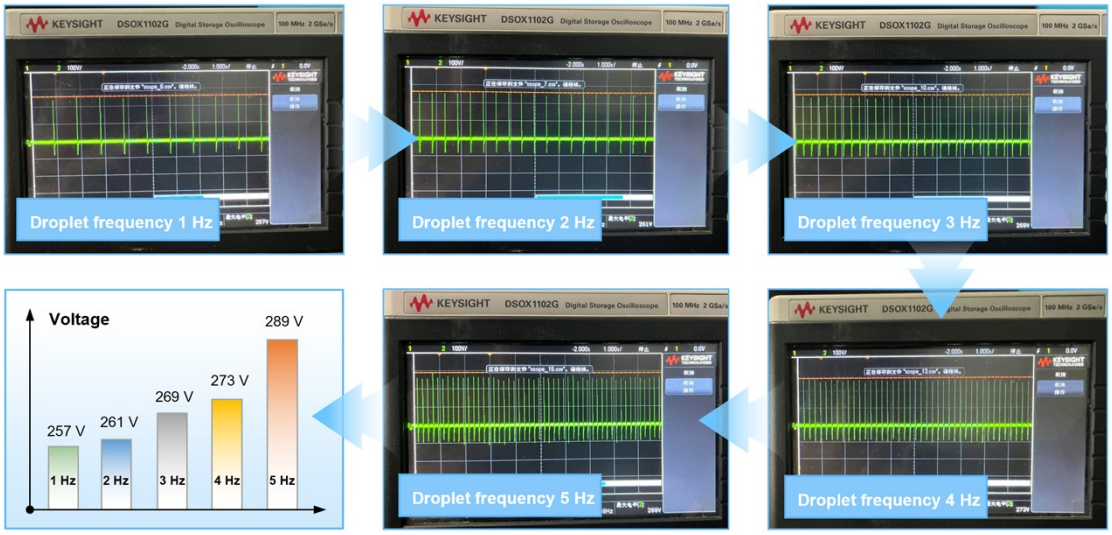

Fig. S28. Voltage curves recorded by an oscilloscope at different droplet frequencies.

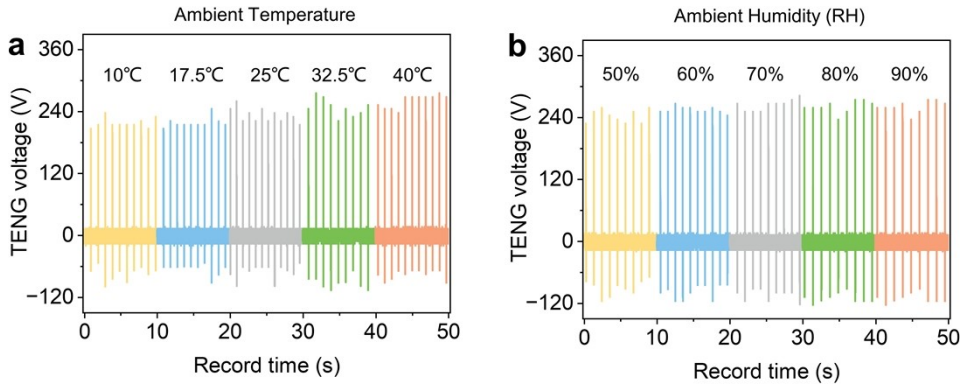

Fig. S29. Temperature and humidity dependency testing of TENG. (a) TENG voltage output at different temperatures; (b) TENG voltage output at different humidities.

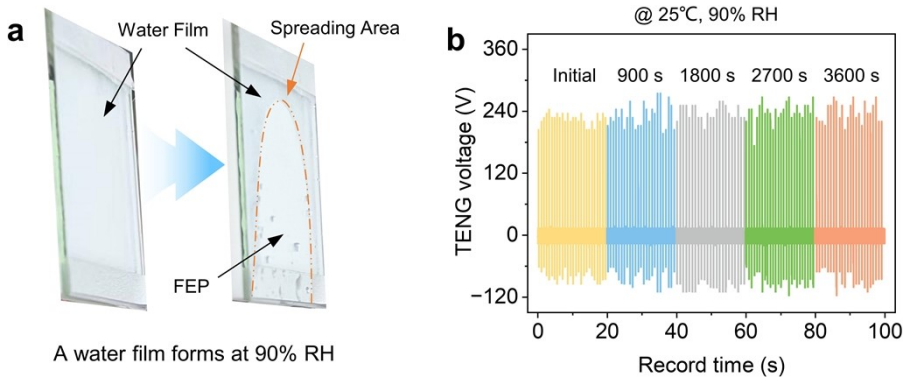

Fig. S30. TENG durability testing for 3600 seconds in a 90 % RH environment. (a) Photograph of the water film on TENG; (b) Voltage curves of TENG at different test times.

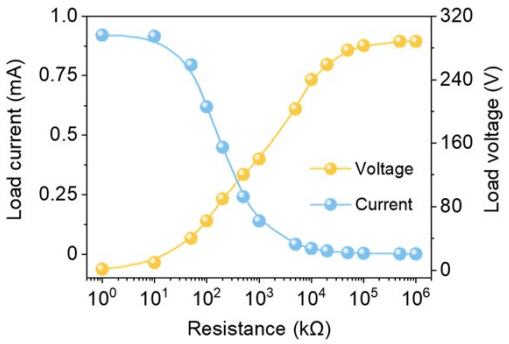

Fig. S31. Voltage and current curves of TENG under different load resistances.

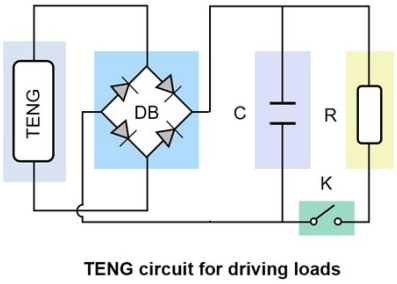

Fig. S32. Circuit of the TENG.

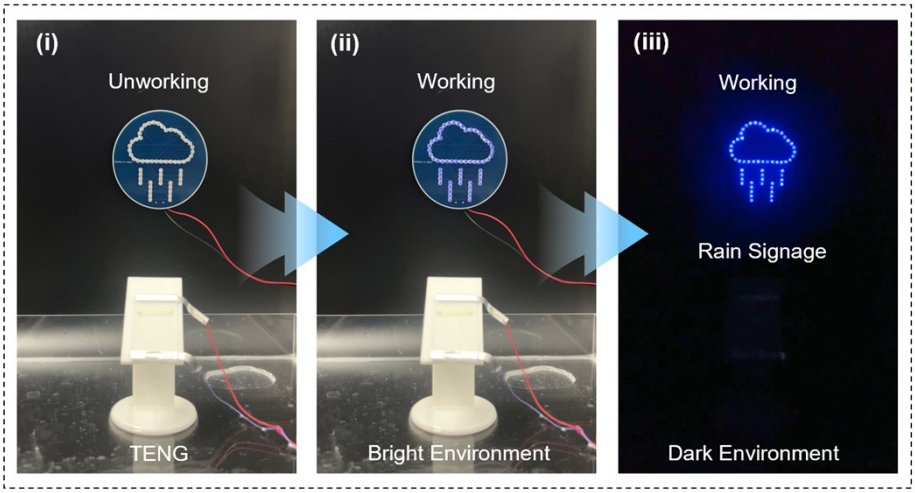

Fig. S33. Application of a rainfall indicator board with 58 LEDs in series illuminated by TENG.

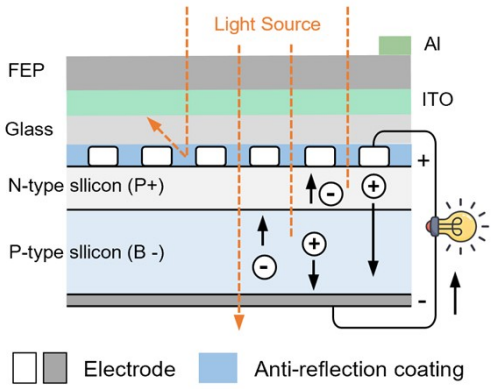

Fig. S34. Integration diagram of TENG and PV.

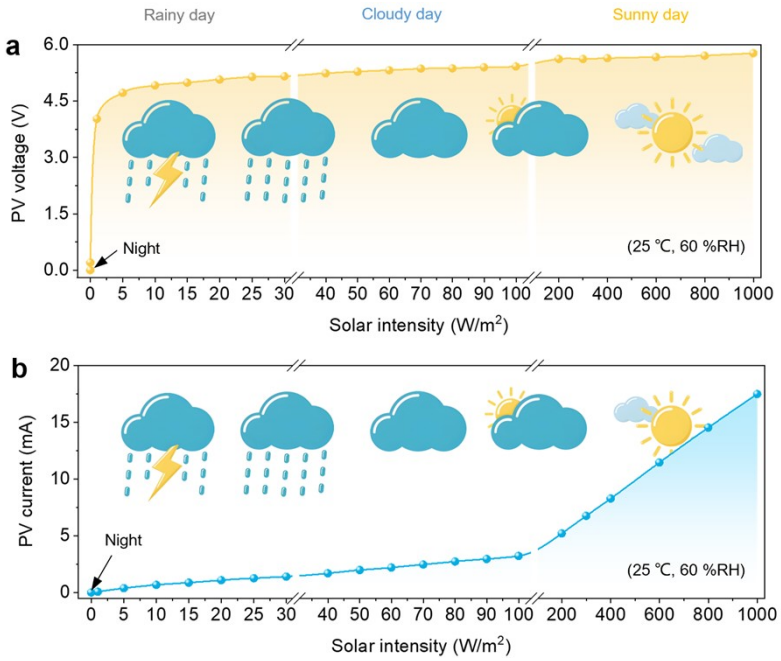

Fig. S35. Output of a single PV module integrated with TENG under different light intensities. (a) Voltage of different light intensities; (b) Current of different light intensities.

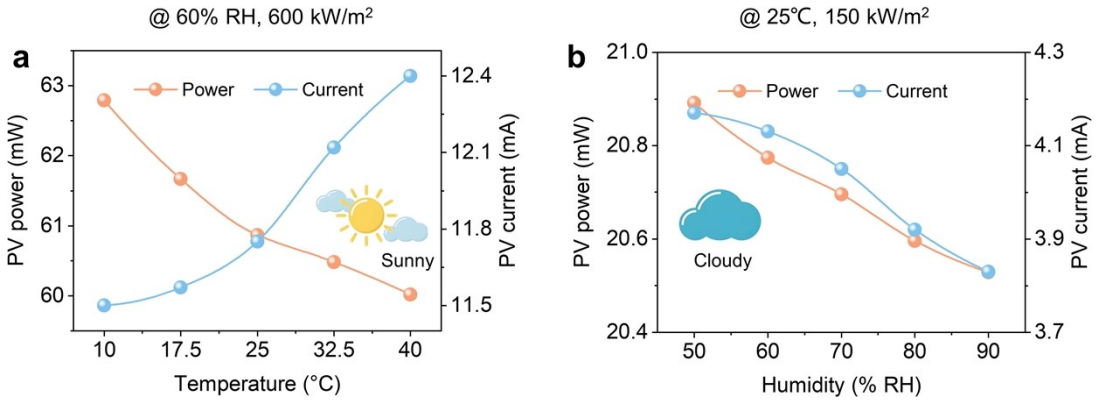

Fig. S36. Temperature and humidity dependency testing of PV. (a) PV power and current output at different temperatures; (b) PV power and current output at different humidities.

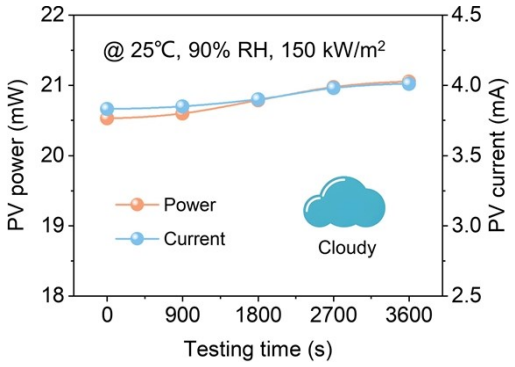

Fig. S37. PV durability testing for 3600 seconds in a 90 % RH environment.

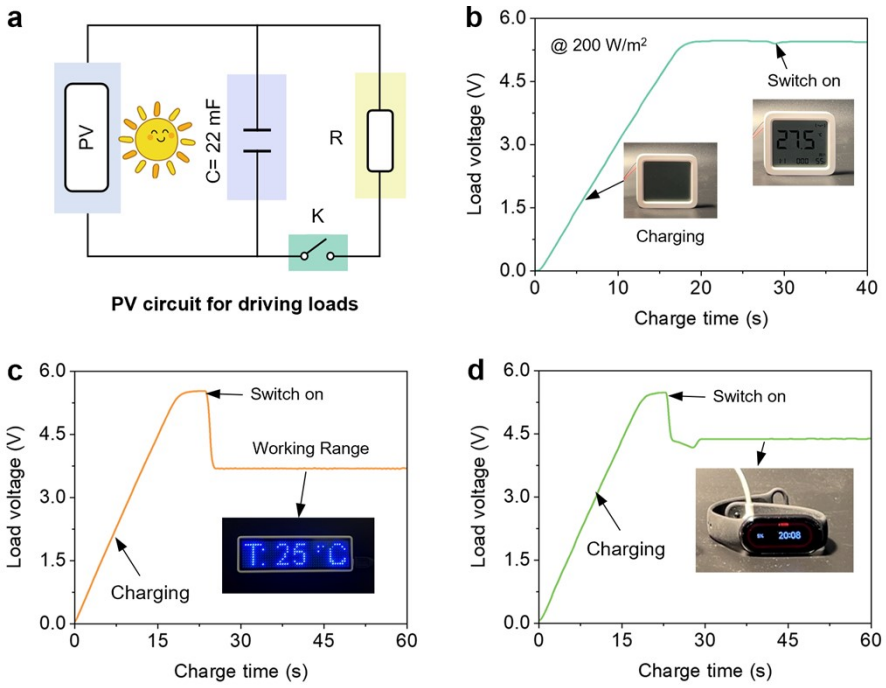

Fig. S38. Application demonstration of a single PV cell. (a) Circuit ; Voltage curves of PV driving a (b) Bluetooth thermo-hygrometer, (c) LED display screen, (d) electronic wristband under 200 W/m² illumination intensity.

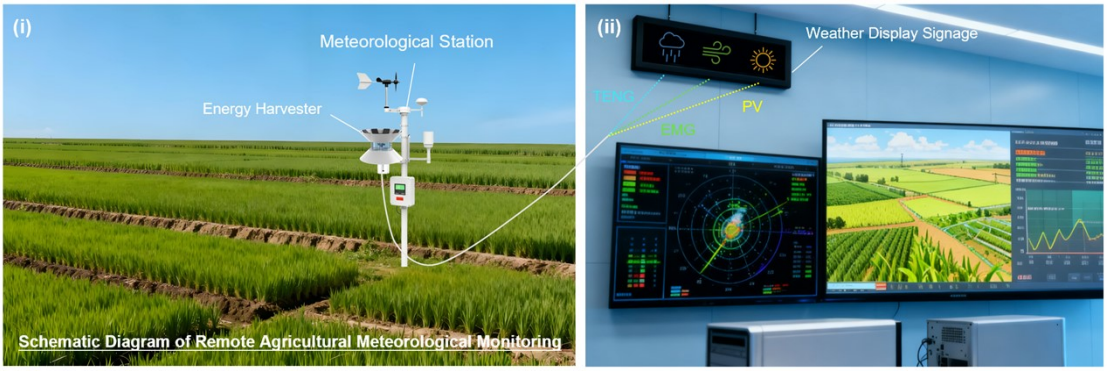

Fig. S39. Conceptual diagram of WSR-EH as a power supply for a remote meteorological indicator board.

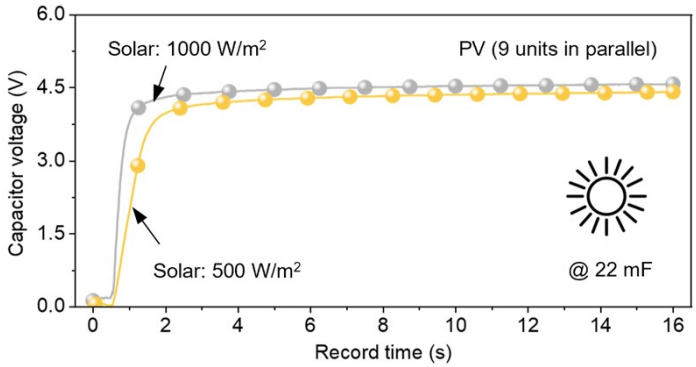

Fig. S40. Voltage curves of capacitor charging for WSR-EH under different light intensities.

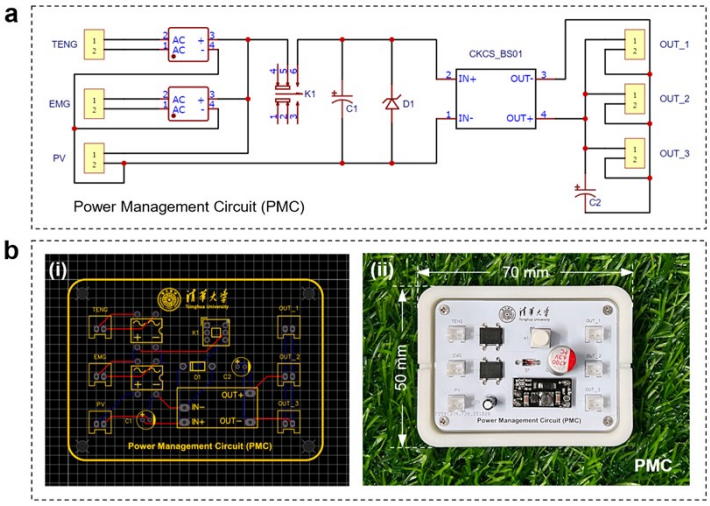

Fig. S41. PMC for WSR-EH. (a) Circuit diagram; (b) PCB layout and physical diagram.

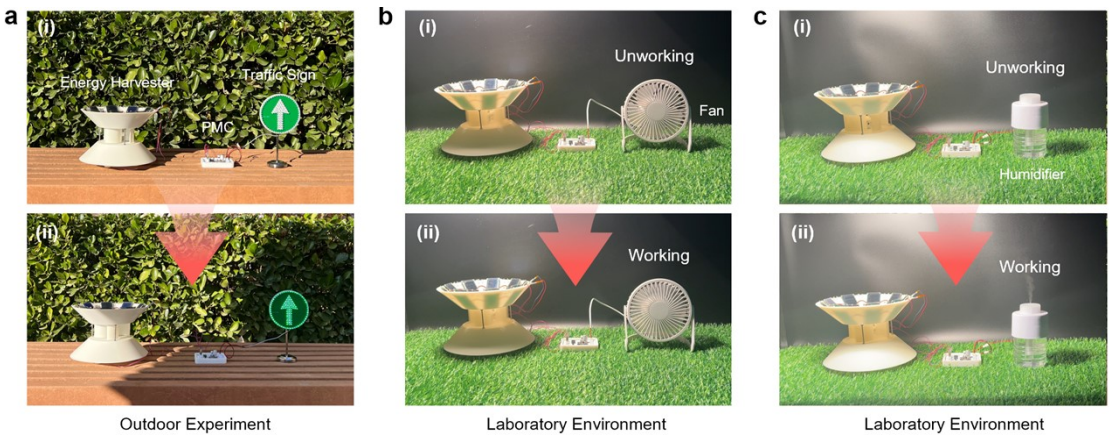

Fig. S42. Outdoor and laboratory power supply applications for WSR-EH. (a) Application of driving straight-ahead traffic signs under outdoor conditions; Demonstration of driving (b) a 5 V small fan and (c) a 5 V humidifier in a laboratory environment.

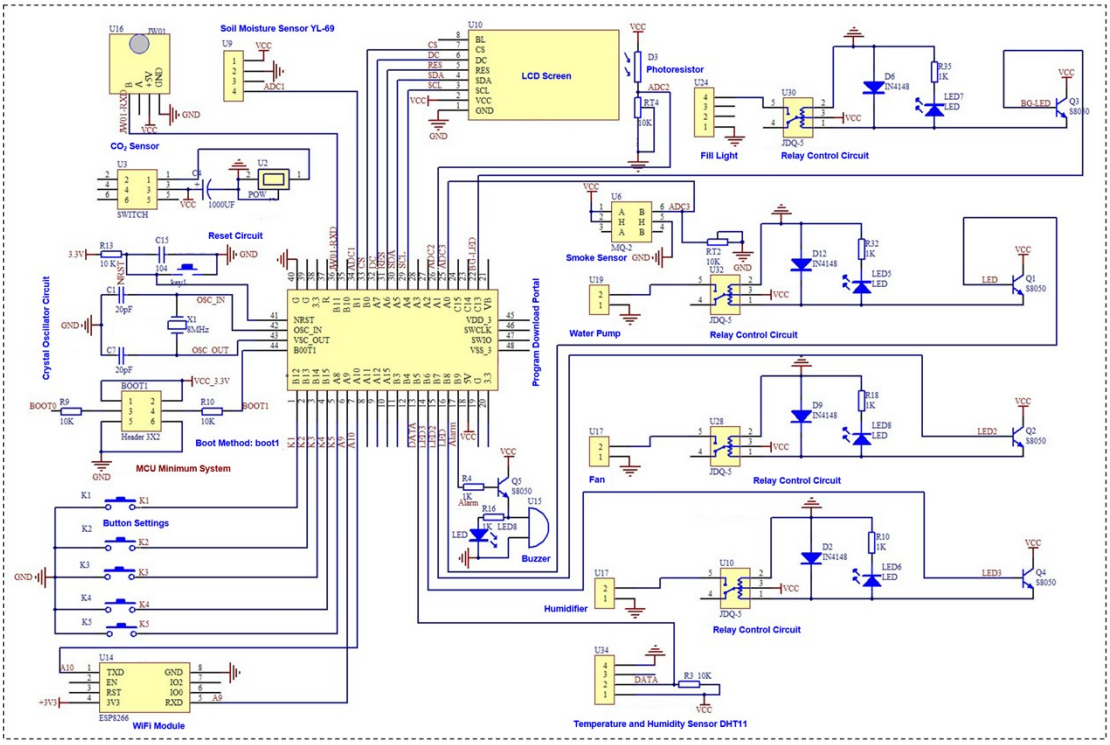

Fig. S43. Smart greenhouse circuit diagram.

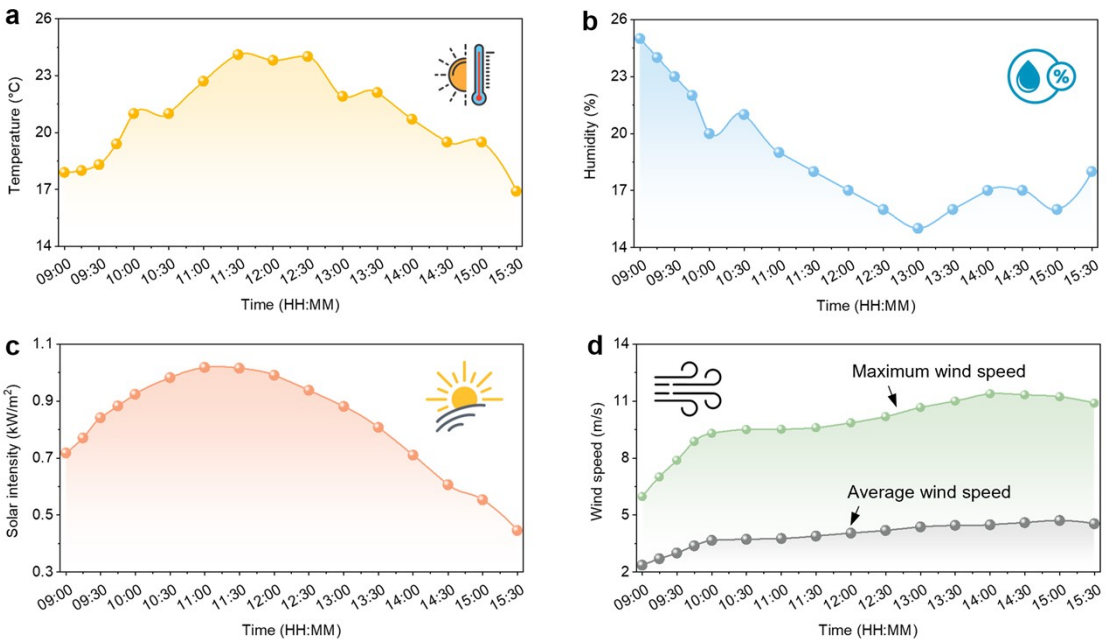

Fig. S44. Environmental parameters during outdoor charging tests of lithium batteries. (a) Ambient temperature; (b) Ambient humidity; (c) Light intensity; (d) Wind speed range.

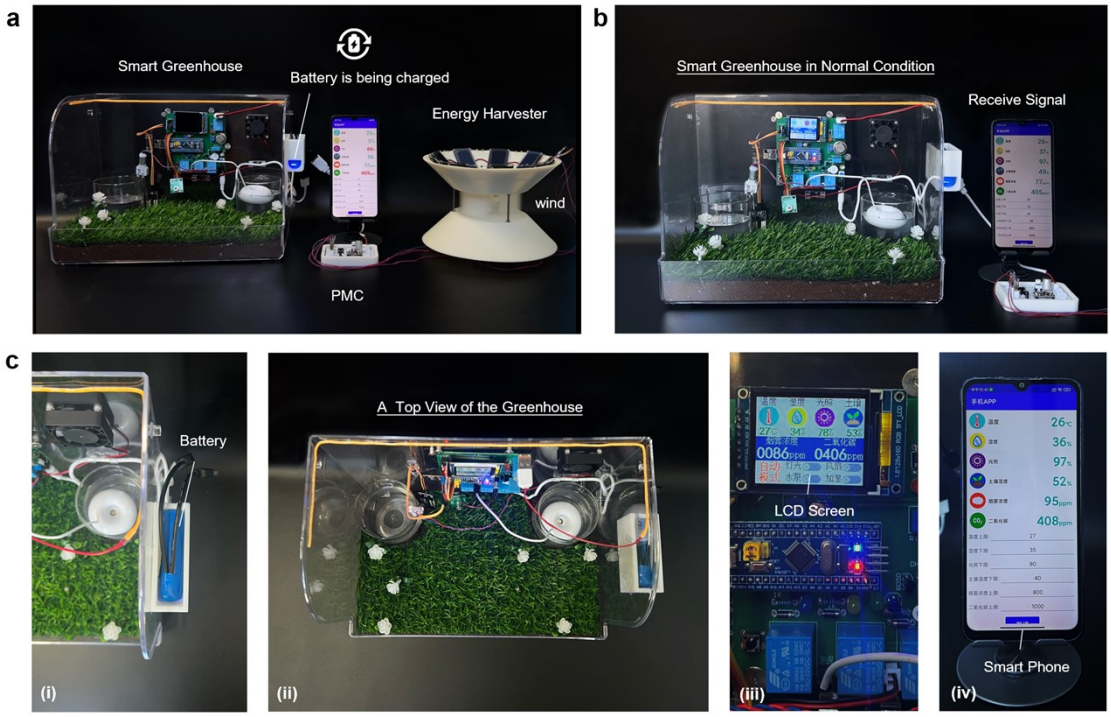

Fig. S45. WSR-EH-powered smart greenhouse. (a) Demonstration of WSR-EH powering the smart greenhouse; (b) Demonstration of the greenhouse under normal environmental parameters; (c) Detailed view of the smart greenhouse.

Table S1. Comparison of WSR-EH with literature in terms of start-up wind speed, peak power density, and energy adaptability.

References	Start-up wind speed	Peak power density	Energy
Ref.58	3.5 m/s	TENG (1.91 W/m^2)	Wind
Ref.45	/	TENG (9.85 W/m^2) PV (3.03 W/m^2)	Wind Solar
Ref.41	3.3 m/s	TENG (0.47 W/m^2) EEH (0.767 W/m^2)	Wind Electric-field
Ref.63	2.2 m/s	TENG (0.0907 W/m^2)	Wind
Ref.60	3.77 m/s	TENG (10.5 W/m^2)	Wind
Ref.61	2 m/s	TENG+EMG (22.39 W/m^2)	Wind
Ref.62	1 m/s	TENG (23.9 W/m^2)	Wind
Ref.59	1.3 m/s	TENG (4.72 W/m^2)	Wind
Ref.39	3 m/s	TENG (0.33 W/m^2)	Wind
Ref.42	2.3 m/s	TENG+EMG (13.3 W/m^2) EEH (0.0394 W/m^2)	Wind Electric-field
Ref.11	2.2 m/s	MEG (11.39 W/m^2)	Wind
Ref.57	3 m/s	TENG (1.24 W/m^2)	Wind
Ref.38	0.32 m/s	/	Wind
Ref.49	0.5 m/s	TENG (1.525 W/m^2) TENG (0.494 W/m^2)	Wind Rain
Ref.43	/	TENG+EMG (0.25 W/m^2) PV (29.3 W/m^2)	Wind Solar
Ref.48	/	TENG (6.18 W/m^2)	Rain
Ref.34	1.3 m/s	TENG (0.178 W/m^2)	Wind
Ref.64	6 m/s	W-TENG (2.65 mW /m^2) R-TENG (13.27 mW/m^2)	Wind Wave Energy
Ref.15	/	TENG (15.03 W/m^2)	Rain
This work	0.4 m/s	EMG (14.158 W/m^2) PV (63.47 W/m^2) TENG (25.42 W/m^2)	Wind Solar Rain

Table S2. A comparison of modular design and traditional stacked design.

References	Power (W/m^2)	Start-up capability	Characteristics
Ref.49	Wind (1.525) Rain (0.494) Peak power	0.5 m/s No optimization	TENG adheres to the spiral blades, and the blade rotation disrupts raindrops.
Ref.65	Wind (0.0254) Wave (0.56) Average power	10 m/s No optimization	Those are two separate, non-contacting units that are bulky and lack integration.
Ref.45	Wind (9.85) Solar (3.03) Peak power	15 m/s No optimization Limited direction	PV stacked on the surface of horizontal TENG, causing easy dust accumulation.
This work	Wind (14.158) Solar (63.47) Rain (25.42) Peak power	0.6→0.4 m/s Reduced by 33.3 % via BcFA	Module integration is based on BcFA. Wind power increases via BcFA by 86.87 %, TENG transmittance is 84.3 %.

[a] In Ref. 49, the raindrop modules need to be bent and stacked on the wind blades. When rotating, the blades interfere with the power generation of the raindrops.

[b] In Ref. 65, the wind-wave module is not structurally integrated. The two components are essentially independent and bulky.

[c] In Ref. 45, the horizontally stacked wind-solar design is prone to dust accumulation. This also results in insufficient utilization of droplet kinetic energy, and the wind-induced vibration TENG is limited by wind direction.

[d] In our design, integration between modules is achieved through BcFA. The inclined surface of the BcFA provides a natural integration platform for PV and TENG. The inclined design not only addresses dust accumulation and liquid residue issues but also simultaneously increases the flow speed of EMG blades (by 36.2 %) and power output (by 86.87 %).

Table S3. Comparison of the results of the flow around a cylinder.

	Norberg[R3]	Jiang[R4]	Dong[R5]	This work
S_t	0.202	0.197	0.209	0.208
C_D	/	1.19	1.11	1.12

Table S4. Parameters for EMG theoretical calculations.

Parameters	Symbol	Units	Values
External wind speed	U_0	m/s	5
Rotor power coefficient	ϑ	1	0.42
Rotational radius of the blade	R	mm	46
Blade drag coefficient	C_D	1	1.2
Number of coil turns	n	1	4400
Magnetic flux density	B	T	0.063
Inner radius of the coils	r_c	mm	1
Outer radius of the coils	R_c	mm	7
Magnet radius	R_m	mm	6
Magnet thickness	h	mm	4
Equivalent pitch between coil and magnet	d	mm	7
Coil number in series	m_1	1	8
Magnet number on the turntable	m_0	1	8

Table S5. Selection criteria for the inclination angle of BcFA in WSR-EH.

α	η of EMG	TENG Voltage	DDD[67]	Peak α= 90°-α_{SN} (Beijing, 40°N)[69]
0°	1			
10°			5.3 g/m^2	
15°	1.258	225.67 V		
16.5°				Summer
20°			4.5 g/m^2	
30°	1.386	250.45 V	3.7 g/m^2	
40°			3.2 g/m^2	
45°	1.344	256.97 V		
50°			2.7 g/m^2	
60°	1.252	240.01 V	2 g/m^2	
63.5°				Winter
75°	1.196	200.88 V		
90°			0.5 g/m^2	

[a] Increasing the inclination angle can reduce surface droplet residue on the TENG, thereby suppressing dust accumulation and adsorption.

[b] DDD is inversely proportional to light transmittance. The smaller the inclination angle, the larger the DDD, and the lower the light transmittance. Since light transmittance directly affects effective irradiance, an increase in DDD will result in a decrease in PV output power.

[c] The test site is located at 40° north latitude. Taking into account both the annual solar irradiance and dust accumulation, the optimal installation angle for the PV system is approximately 40°.

Note S1 Governing Equations for Large Eddy Simulation (LES)

Currently, common numerical simulation techniques used in flow field analysis include Direct Numerical Simulation (DNS)[R1], Reynolds-Averaged Numerical Simulation (RANS)[R2], and Large Eddy Simulation (LES)[66]. In this work, CFD (Computational Fluid Dynamics) analysis is performed on BcFA using the LES method. The focus of LES lies in depicting the motion and development process of large-scale vortices. When performing LES, spatial filtering must be applied to the unsteady Navier-Stokes (N-S) equations to resolve the effects of large-scale vortices in the computations. Subsequently, utilizing the subgrid-scale model, the indirect effects of small-scale vortices on large-scale vortices are approximated.

LES divides flow into large-scale and small-scale components:

$$\Upsilon = \overline{\Upsilon} + \Upsilon' \tag{1}$$

where $\overline{\Upsilon}$ is large-scale vortices, Υ' is small-scale vortices.

The filter function is:

$$G(x,x') = \begin{cases} \dfrac{1}{V}, x' \in V \\ 0, x' \notin V \end{cases} \tag{2}$$

where V represents the volume of the computational unit.

The filtering velocity is obtained from the filtering function $G(x,x')$:

$$\overline{u}_i = \int_D u_i G(x,x') dx' \tag{3}$$

Substituting Equation (3) into the three-dimensional incompressible N-S equations yields the governing equations for spatially averaged LES:

$$\frac{\partial \overline{u}_i}{\partial x_i} = 0 \tag{4}$$

$$\frac{\partial \overline{u}_i}{\partial t} + \frac{\partial \overline{u}_i \overline{u}_j}{\partial x_j} = -\frac{1}{\rho}\frac{\partial \overline{p}}{\partial x_i} + v\frac{\partial^2 \overline{u}_i}{\partial x_i \partial x_j} - \frac{\partial \tau_{ij}}{\partial x_j} \tag{5}$$

where ρ is the fluid density, v is the kinematic viscosity, t is time; $\overline{u}_i$ and $\overline{u}_j$ represent the large-scale components of the flow along the x and y directions, respectively; x_i and x_j are the components in the coordinate directions,

$\overline{p}$ is the filtered pressure; τ_{ij} is the subgrid-scale stress tensor, $\partial \tau_{ij} / \partial x_j$ represents the influence of small-scale vortices on large-scale vortices in turbulent flow.

The subgrid-scale stress tensor of the Smagorinsky-Lilly model is:

$$\tau_{ij} - \frac{1}{3}\tau_{kk}\delta_{ij} = -2\mu_t \overline{S}_{ij} \tag{6}$$

where τ_{kk} is the sublattice turbulent energy, μ_t is the turbulent viscosity coefficient, δ_{ij} is the Kronecker delta function, $\overline{S}_{ij}$ is the strain rate tensor.

The expressions for $\overline{S}_{ij}$ and μ_t are as follows:

$$\overline{S}_{ij} = \frac{1}{2}\left(\frac{\partial \overline{u}_i}{\partial x_j} + \frac{\partial \overline{u}_j}{\partial x_i}\right) \tag{7}$$

$$\mu_t = \rho L_s^2 \sqrt{2\overline{S}_{ij}\overline{S}_{ij}} \tag{8}$$

L_s is the hybrid length at the submesh scale:

$$L_s = \min(kd, C_s V^{1/3}) \tag{9}$$

where k is the Von Kármán constant, d is the distance from the computational cell to the nearest wall, and C_s is the Smagorinsky constant.

Note S2 Mesh optimization and reliability verification of the simulation model

As shown in Fig. S5, the computational domain boundary conditions are set as velocity-inlet (U_0), pressure-outlet, and no-slip wall. The computational domain dimensions are: length 1800 mm, width 1000 mm, height 1000 mm. The volume-center of the BcFA model is 300 mm from the inlet and 500 mm from the side boundary. The model employs a free tetrahedral mesh partitioning. The mesh is refined around the BcFA, while coarse meshes are used at the far ends to enhance computational efficiency and accuracy. The model is solved by a transient solver with a calculation time of 5 s and a time step of 0.0001 s.

To validate the accuracy of the numerical simulation, the grid refinement of the model is optimized first. As shown in Fig. S6, three grid resolutions are selected: sparse grid (1415470 cells), medium grid (2612043 cells), and dense grid (3551072 cells). In the three mesh configurations, the calculated average flow speeds at the blade position in plane-B are 6.57 m/s, 6.72 m/s, and 6.722 m/s, respectively. Given the high computational cost associated with dense grids, the medium grid density is selected for subsequent studies.

To further validate the reliability of the model, simulations of the classical flow around a cylinder are conducted. The Reynolds number used for validation is 10000. The dimensionless coefficients employed for verification include the Strouhal number S_t and the drag coefficient C_D. As shown in Table S3, the computational results of the model closely match those reported in the literature. This indicates that the established simulation model is feasible in terms of accuracy and reliability.

Note S3 The flow-speed amplification ratio model of the BcFA

As shown in Fig. S9, the flow acceleration performance of a traditional variable-section structure is determined by the inclination angle α, the hypotenuse length L, and the plane distance K. Since the structure is enclosed, it satisfies the boundary condition for the dominant flow direction, which requires streamlines to converge. In this case, the flow satisfies the law of energy conservation[R10]:

$$P_0 + \frac{1}{2}\rho U_0^2 + \rho g h_0 = P_1 + \frac{1}{2}\rho U_1^2 + \rho g h_1 \tag{10}$$

where P_0 and $P1$ are the static pressures before and after acceleration, g is the gravity acceleration, and h_0 and h_1 are the fluid heights.

According to the continuity equation, the volumetric flow rate through different cross-sections obeys the law of conservation[R10]:

$$A_0 U_0 = A_1 U_1 \tag{11}$$

where A_0 and A_1 are the cross-sectional areas.

Therefore, the flow-speed amplification ratio for a closed structure can be calculated as:

$$\eta = \frac{U_1}{U_0} = 1 + (2L/K)\sin\alpha \tag{12}$$

In this study, the BcFA has a semi-enclosed structure. As the airflow passes through the BcFA, escape flow is generated. Since this portion of the flow does not enter the gap, the flow speed U_1 is lower than the value predicted by Equation (12). Therefore, we introduce a corrected empirical coefficient c to adjust the above equation:

$$\eta = \frac{U_1}{U_0} = 1 + c(2L/K)\sin\alpha \tag{13}$$

The coefficient c is used to describe the escape of airflow. As shown in Figs. 2b–g and Fig. S10, its value depends on L, K, and α. Because direct measurement of the escape flow is currently not possible, we obtained average flow speed results for specific structural parameters based on CFD simulations

(Fig. S11). Next, the value of c under different geometric conditions was obtained using Equation (13). Using this value as the theoretical value, an empirical relationship between c and the structural parameters was established:

$$c = 0.5e^{-0.0265\alpha} K^{0.43} L^{-0.37} \tag{14}$$

The validity of this model can be verified by comparing the flow speeds predicted by the formula with the measured results. As shown in Fig. 2i, the two show excellent agreement, demonstrating the reliability of Equation (13). Furthermore, this also validates the validity of the coefficient c in Equation (14). This is because the other parameters in the equation are measurable values. Fig. S12 shows that the values of c calculated using Equation (14) exhibit excellent agreement with simulation and experimental data. Specifically, the empirical formula not only captures the relationship between c and structural parameters but also demonstrates high numerical accuracy.

Note S4 Force-induced rotational generation theory model of EMG

As shown in Fig. S14, a vertical-axis blade is installed at the structural gap of the BcFA. The blade will rotate under the action of airflow (U_1). The driving force acting on the blade is:

$$F_D = 0.5 C_D \rho A U_1^2 \tag{15}$$

where C_D is the drag coefficient, and A is the wind-exposed area of the blade.

Under the action of the driving force, the driving torque M of the EMG is:

$$M = F_D R \tag{16}$$

where R is the rotational radius of the blade.

For vertical-axis systems, the input power gained by the blades from the airflow is[R6]:

$$P_{in} = 0.5 \rho S U_1^3 \vartheta \tag{17}$$

where ϑ is the rotor power coefficient.

On the other hand, the power can also be expressed in terms of torque and rotational speed:

$$P_{in} = M \omega \tag{18}$$

where ω is the rotational speed (unit: 1/s, i.e., rad/s).

Combining Equation (15) to Equation (18) yields the rotational speed:

$$\omega = 0.5 \rho A U_1^3 \vartheta / F_D R = U_1 \vartheta / R C_D \tag{19}$$

According to the law of electromagnetic induction, the induced voltage in a single cylindrical coil is:

$$V = nBS\omega = nBSU_1 \vartheta / R C_D \tag{20}$$

where n is the number of coil turns, S is the coil area, and B is the magnetic flux density.

For a cylindrical magnet, the magnetic flux density generated in the cylindrical coils is:

$$B = \frac{B_r}{2}\left(\frac{d+h}{\sqrt{(d+h)^2 + r^2}} - \frac{d}{\sqrt{d^2 + r^2}} \right) \tag{21}$$

where B_r is the residual magnetic flux density, d is the equivalent distance between the coil and magnet, h is the magnet thickness, and r is the magnet radius.

From Equation (20), it is observed that the EMG voltage is positively proportional to the flow speed. Therefore, the voltage enhancement ratio of the EMG after introducing BcFA corresponds to the flow-speed amplification ratio:

$$\frac{V_1}{V_0} \approx \frac{U_1}{U_0} = \eta = 1 + c\left(2L / K\right)\sin\alpha \tag{22}$$

As the magnet rotates with the blade, the area of direct alignment between the magnet and the coils varies sinusoidally. Therefore, the dynamic output voltage V_1 can be expressed as:

$$V_1 = \frac{nm_1 BSU_1 \vartheta}{RC_D}\sin(\frac{m_0 U_1 \vartheta}{RC_D}t) \tag{23}$$

where m_0 denotes the magnet number on the turntable, and m_1 denotes the number in series.

Note S5 Force analysis and contact expansion of droplet TENG

As shown in Fig. S15, assuming the raindrop is a sphere with volume V_d, the droplet diameter D_d is:

$$D_d = (6V_d / \pi)^{1/3} \tag{24}$$

The descent of the raindrop is influenced by the forces of gravity (F_G), buoyancy (F_B), and drag (F_D):

$$F_G = \rho_d V_d g \tag{25}$$

$$F_B = \rho_a V_d g \tag{26}$$

$$F_D = 0.5 C_D \rho_a A_d v^2 \tag{27}$$

where ρ_d is the density of the droplet, g is the gravitational acceleration, ρ_a is the density of air, $A_d = \pi D_d^2/4$ is the effective wind-exposed area of the droplet, v is the instantaneous velocity of the droplet.

When the three forces are in equilibrium, the raindrop moves with uniform linear velocity. The corresponding droplet velocity is defined as the terminal velocity v_t. The equation of motion for a falling droplet can be written as:

$$\rho_d V_d \frac{dv}{dt} = (\rho_d - \rho_a) V_d g - 0.5 C_D \rho_a A_d v^2 \tag{28}$$

Let $g' = \frac{\rho_d - \rho_a}{\rho_d} g$, and substitute A_d and V_d into Equation (28):

$$\frac{dv}{dt} = g' - \beta v^2, \beta = \frac{3 C_D \rho_a}{4 \rho_d D_d} \tag{29}$$

When $d_v/d_t = 0$, the terminal velocity can be determined:

$$v_t = \sqrt{\frac{g'}{\beta}} = \sqrt{\frac{4(\rho_d - \rho_a) g D_d}{3 C_D \rho_a}} \tag{30}$$

On the other hand, it is necessary to calculate the relationship between the droplet impact velocity and droplet height (H). From $d_v/d_t = d_v/d_y \cdot d_y/d_t = v d_v/d_y$, we obtain the equation of motion $v dv / dy = g' - \beta v^2$. After separating the variables, integrate:

$$\int_0^{v_i} \frac{v}{g' - \beta v^2} dv = \int_0^H dy \tag{31}$$

where y is the falling distance.

Let $w = g' - \beta v^2$, $dw = -2\beta v dv$, so $v dv = -dw / 2\beta$. The integral on the left-hand side of Equation (31) is:

$$\int_{g'}^{g'-\beta v^2} \frac{-dw/2\beta}{w} = -\frac{1}{2\beta}\int_{g'}^{g'-\beta v^2} \frac{dw}{w} = -\frac{1}{2\beta}\left[\ln|w|\right]_{g'}^{g'-\beta v^2} = -\frac{1}{2\beta}\ln\left(\frac{g' - \beta v^2}{g'}\right) \tag{32}$$

The integral on the right-hand side of Equation (31) is H. Then Equation (31) can be further written as:

$$-\frac{1}{2\beta}\ln\left(\frac{g' - \beta v^2}{g'}\right) = H \tag{33}$$

Equation (33) can be further simplified to:

$$\ln\left(1 - \frac{\beta v^2}{g'}\right) = -2\beta H \rightarrow 1 - \frac{\beta v^2}{g'} = e^{-2\beta H} \tag{34}$$

Therefore, the formula for calculating the droplet impact speed is:

$$v_h^2 = \frac{g'}{\beta}(1 - e^{-2\beta H}) \tag{35}$$

Since $v_t = \sqrt{g'/\beta}$, the impact speed can be expressed as:

$$v_i = v_t\sqrt{(1 - e^{-2\beta H})} = v_t\sqrt{(1 - \exp\left(-\frac{2g'H}{v_t^2}\right))} \tag{36}$$

From Equation (36), it can be observed that when the droplet height is sufficiently high ($H \rightarrow \infty$), the droplet impact velocity (v_i) equals the terminal velocity (v_t). When H is small, the impact velocity is the velocity of free fall.

When a droplet impacts the TENG, it will spread across the FEP film surface. The maximum spread area during the droplet spreading process is denoted as S_D. The following assumptions are made for calculating S_D:

(i) The volume of the droplet remains constant before and after spreading.

(ii) Neglecting energy losses such as viscous dissipation and vibration, all kinetic energy is converted into an increase in surface energy.

(iii) At maximum spreading, the droplet assumes a cylindrical shape (radius R_D, height h_D), with a contact angle θ equal to the equilibrium contact angle on the FEP film.

(iv) Changes in solid surface energy are described by the Young equation: $\gamma_{SV}=\gamma_{SL}+\gamma_{LV}\cos\theta$. $\gamma_{SV}$is the solid-vapor interfacial tension, γ_{SL} is the solid-liquid interfacial tension, and γ_{LV} is the liquid-vapor surface tension.

(v) Conservation of Energy: Initial total energy (kinetic energy + initial surface energy) = surface energy at maximum spreading.

The initial surface energy comprises the liquid-vapor surface energy ($4\pi R_d^2\gamma_{LV}$, where R_d is the droplet radius) and the solid-vapor surface energy ($\gamma_{SV}A_{soid}$). At maximum spreading state, the surface energy comprises solid-liquid interfacial energy ($\gamma_{SL}\pi R_D^2$) and liquid-vapor interfacial energy (top surface: $\gamma_{LV}\pi R_D^2$, side surfaces: $\gamma_{LV}\cdot 2\pi R_D h_D$).

Therefore, the initial total surface energy associated solely with the droplet is:

$$E_{initial}= 4\pi R_d^2\gamma_{LV} + \gamma_{SV}A_{solid} \tag{37}$$

At the maximum spreading of the droplet, the total surface energy is:

$$E_{final}= \gamma_{LV}(\pi R_D^2 + 2\pi R_D h_D) + \gamma_{SL}\pi R_D^2 + \gamma_{SV}(A_{solid} - \pi R_D^2) \tag{38}$$

Hence, the change in surface energy ΔE_s is:

$$\Delta E_s = E_{final} - E_{initial}= \gamma_{LV}(\pi R_D^2 + 2\pi R_D h_D) + \gamma_{SL}\pi R_D^2 - \gamma_{SV}\pi R_D^2) - 4\pi R_d^2\gamma_{LV} \tag{39}$$

Using the Young equation and the conservation of droplet volume (V_d= $\pi R_D^2 h_D$= $4\pi R_d^3/3$), an expression for h_D is derived. Subsequently, substitute it into Equation (39) to obtain ΔE_s:

$$\Delta E_s = \gamma_{LV}\left(\pi {R_D}^2(1-\cos\theta) + \frac{8\pi R_d^3}{3R_D}\right) - 4\pi R_d^2\gamma_{LV} \tag{40}$$

On the other hand, the kinetic energy of the droplet is:

$$E_k = \frac{1}{2}\rho_d V_d v_h^2 \tag{41}$$

According to the law of conservation of energy, E_k=ΔE_s, then we have:

$$\frac{2}{3}\pi R_d^3 \frac{\rho_d v_h^2}{\gamma_{LV}} = \pi R_D{}^2 \left(1-\cos\theta\right) + \frac{8\pi R_d^3}{3R_D} - 4\pi R_d^2 \tag{42}$$

Using the introduced dimensionless spreading radius ξ (ξ=R_D/R_d) and Weber number We (We=$\rho_d D_d v_h{}^2/\gamma_{LV}$), Equation (42) is simplified to:

$$\frac{We}{3} + 4 = \xi^2 \left(1-\cos\theta\right) + \frac{8}{3\xi} \tag{43}$$

Generally, at the maximum spreading state, $\xi \gg 1$, so the $8/3\xi$ term can be neglected (being small relative to ξ^2):

$$\xi^2 \approx \frac{We+12}{3\left(1-\cos\theta\right)} \tag{44}$$

Using R_d=D_d/2, $V_d = \pi D_d^3/6$, and Equation (44) to process the maximum spread area ($S_D = \pi R_D^2 = \pi \xi^2 R_d^2$):

$$S_D = \pi \cdot \frac{\rho_d D_d v_h{}^2 + 12\gamma_{LV}}{3\gamma_{LV}\left(1-\cos\theta\right)} \cdot \frac{D_d^2}{4} = \frac{\pi\rho_d D_d^3 v_h{}^2 + 12\pi\gamma_{LV} D_d^2}{12\gamma_{LV}\left(1-\cos\theta\right)} = \frac{\rho_d V_d v_h{}^2 + 2\pi\gamma_{LV} D_d^2}{2\gamma_{LV}\left(1-\cos\theta\right)} \tag{45}$$

It can be found from Equation (45) that S_D is closely related to v_h, which in turn affects charge transfer. When TENG is mounted at an angle α to BcFA, the effective impact speed is $v_h\cos\alpha$. Generally, increasing the droplet volume/ height or decreasing the contact/inclination angle is beneficial for enhancing TENG output. This provides a theoretical basis for subsequent experimental result analysis.

Note S6 Circuit model of droplet TENG

As shown in Fig. S16a(i), a dielectric capacitor C_F forms at the FEP/ITO electrode interface before the droplet falls onto the FEP surface. When the droplet contacts FEP, an electrical double-layer capacitor (EDLC) forms at the liquid-solid interface. As depicted in Fig. S16a(i) and Fig. S16b, the circuit is "switch-off" before the droplet contacts the top AI electrode. C_{E1}, R_D, and R_L represent the EDLC at the droplet-FEP interface, the droplet resistance, and the external resistance, respectively. As shown in Fig. S16a(ii), when the droplet contacts the AI electrode, another EDLC (C_{E2}) forms at the droplet-AI electrode interface, causing the circuit to enter the "turn-on" state (see Fig. S16c). In this state, charge will be released from C_F to C_{E1} and C_{E2}. As shown in Fig. S16a(iii), when the droplet shrinks, the C_F capacitor is charged by C_{E1} and C_{E2}. Finally, when the droplet slides off the top AI electrode, the circuit reverts to the "switch-off" state, as shown in Fig. S16a(iv). In this process, the droplet can be regarded as the switch of the circuit.

In the circuit model, the three capacitances can be calculated by:

$$C_F(t) = d_{FEP} A_1(t) \varepsilon_F \tag{46}$$

$$C_{E1}(t) = \frac{A_1(t)\varepsilon_w}{\lambda_{EDL}} \tag{47}$$

$$C_{E2}(t) = \frac{A_2(t)\varepsilon_w}{\lambda_{EDL}} \tag{48}$$

where ε_F and d_{FEP} are the dielectric constant and thickness of FEP, respectively; $A_1(t)$ and $A_2(t)$ represent the contact area between the droplet-FEP interface and the droplet-AI electrode, respectively; ε_w is the dielectric constant of water, and λ_{EDL} is the width of the EDLC.

The circuit can be described by the following differential equation:

$$(R_L + R_D)\frac{dq(t)}{dt} = \frac{Q_F(t) - q(t)}{C_F(t)} - \frac{q(t)}{C_{E1}(t)} - \frac{q(t)}{C_{E2}(t)} \tag{49}$$

$$q(t=0) = 0 \tag{50}$$

Note S7 A PV power generation model considering dust deposition and TENG transmittance

The PV panels integrated into the top slope of the BcFA utilize the photovoltaic effect to convert solar radiation into electrical energy. According to previous work[R7], the standard test condition (STC) for PV is defined as a solar density of 1 kW/m^2, a cell temperature of 25 °C, and a windless environment. The nominal operating cell temperature (NOCT) is defined as the cell temperature with the incident radiation of 0.8 kW/m^2, the ambient temperature of 20 ℃, the average wind speed of 1 m/s, and no load operation. A simple model for predicting the power of a PV array is expressed as[67]:

$$P_{PV} = Y_{PV} f_{PV} \left(\frac{\bar{G}_T}{\bar{G}_{T,stc}} \right) \left[1 + \varphi_P \left(T_C - T_{C,stc} \right) \right] \tag{51}$$

where Y_{PV} is the STC power output of the PV array, and f_{PV} is the PV derating factor accounting for shading, snow load, and aging factors; $\bar{G}_T$ is the global radiation striking the PV array, $\bar{G}_{T,stc}$ is the incident radiation under STC (1 kW/m^2); φ_P is the temperature coefficient of power; T_C is the PV cell temperature in the current time step, and $T_{C,stc}$ is the STC temperature.

T_C can be calculated as:

$$T_C = \frac{T_a + \left(T_{C,NOCT} - T_{a,NOCT} \right) \left(G_T / G_{T,NOCT} \right) \left[1 - \left(\eta_{mp,stc} / \tau\varphi \right) \left(1 - JT_{C,stc} \right) \right]}{1 + \left(T_{C,NOCT} - T_{a,NOCT} \right) \left(G_T / G_{T,NOCT} \right) \left(\eta_{mp,stc} / \tau\varphi \right)} \tag{52}$$

where T_a is the ambient temperature; $T_{C,NOCT}$, $T_{a,NOCT}$, and $G_{T,NOCT}$ represent the NOCT cell temperature, ambient temperature, and solar intensity, respectively; $\eta_{mp,stc}$ is the maximum power point efficiency under STC, τ is the solar transmittance of the PV array, and φ is the solar absorptance of the PV array.

Total solar radiation on a PV panel with an inclination angle of α can be represented by the HDKR model[R8]:

$$\bar{G}_T = \bar{G}_{T,b} + \bar{G}_{T,d} + \bar{G}_{T,refl} \tag{53}$$

where $\bar{G}_{T,b}$ is the beam radiation, $\bar{G}_{T,d}$ is the sum of the diffuse radiation, $\bar{G}_{T,refl}$ is the ground reflected radiation.

The calculation formulas for the three types of radiation are as follows:

$$\bar{G}_{T,b} = \bar{G}_b \cdot R_b = \bar{G}_b \frac{\cos\theta_i}{\cos\theta_z} \tag{54}$$

$$\bar{G}_{T,d} = \bar{G}_d \left(R_b A_i\right) + \bar{G}_d \left(1 - A_i\right)\left(\frac{1+\cos\alpha}{2}\right)\left[1 + f\sin^3\left(\frac{\alpha}{2}\right)\right] \tag{55}$$

$$\bar{G}_{T,refl} = \bar{G} \cdot \rho_r \cdot \left(\frac{1-\cos\alpha}{2}\right) \tag{56}$$

where ρ_r is the albedo coefficient of the ground, $\bar{G}$, $\bar{G}_d$, and $\bar{G}_b$ are the total radiation, the diffuse radiation, and the beam radiation on the horizontal plane, respectively; θ_z is the zenith angle, θ_i is the incident angle, and R_b is the geometric factor; A_i is the forward scattered radiation. f is the correction factor:

$$f = \sqrt{\frac{\bar{G}_b}{\bar{G}}} \tag{57}$$

A_i is the ratio of direct radiation $\bar{G}_b$ to extraterrestrial radiation $\bar{G}_o$ on a horizontal ground:

$$A_i = \frac{\bar{G}_b}{\bar{G}_o} \tag{58}$$

Regarding the solar altitude angle α_S, it is the angle between the light of the sun and the ground, i.e., the complementary angle of the zenith angle. Latitude is the most fundamental geographical factor determining α_S. At noon, the relationship between the solar altitude angle α_{SN} and latitude ϕ and solar declination δ is as follows:

$$\alpha_{SN} = 90° - \left|\phi - \delta\right| \tag{59}$$

The solar declination varies throughout the year, so the α_{SN} in the same region also changes accordingly. For example, in Beijing (40°N), the α_{SN} is high in summer and low in winter.

As shown in Fig. S17, the design objective for the inclination angle is to allow sunlight to strike the PV panel surface as perpendicularly as possible, thereby maximizing the amount of received radiant energy:

$$\alpha = 90° - \alpha_S \tag{60}$$

However, in practice, the α_S fluctuates constantly. Therefore, for PV systems with fixed inclination angles, it is necessary to select a compromise optimal inclination angle to maximize total received radiation over the entire year or during specific periods.

For fixed PV arrays, the rule of thumb indicates that the inclination angle maximizing annual radiation received by PV panels is approximately equal to the local latitude:

$$\alpha_{opt} \approx \phi \tag{61}$$

Note that for PV systems optimized for summer or winter applications, the optimal inclination angle is typically designed to be ±(10°~15°) of the latitude.

Additionally, the zenith angle can be expressed in terms of latitude, solar declination, and the hour angle ω_h:

$$\cos\theta_z = \cos\phi\cos\delta\cos\omega_h + \sin\phi\sin\delta \tag{62}$$

Thus, the total solar radiation on a α tilted surface can be expressed as:

$$\overline{G}_T = R_b\left(\overline{G}_b + \overline{G}_d A_i\right) + \overline{G}_d\left(1 - A_i\right)R_d\left[1 + f\sin^3\left(\frac{\alpha}{2}\right)\right] + \overline{G}\rho_r R_r \tag{63}$$

where R_d= (1+cosα)/2, R_r= (1-cosα)/2.

However, the aforementioned model is applicable only to PV panels with clean surfaces. In practical applications, PV panels are exposed to the air, and dust accumulates on their surfaces over time. The dust deposition causes a significant decrease in light transmittance, thereby substantially suppressing the PV performance.

It has been demonstrated that the dust deposition density (ρ_D, g/m^2) correlates with exposure duration and the inclination angle of PV panels[67]:

$$\rho_D(\alpha) = -8.5\times10^{-3}\rho_{D0}\alpha + 0.82\rho_{D0} \tag{64}$$

where ρ_{D0} is the dust deposition density of α= 0°.

The optimal relationship between dust deposition density and solar

transmittance is[R9]:

$$\Delta\tau = 34.37\mathrm{erf}\left(0.17\rho_D^{0.8473}\right) \tag{65}$$

The formula for calculating transmittance τ is:

$$\tau = \left(1-\Delta\tau\right)\tau_{clean} \tag{66}$$

where τ_{clean} is the transmittance of a clean glass plate, with values ranging from 0.98 to 1.

Moreover, the relationship between light transmittance and inclination angle is:

$$\tau = \left\{-34.37\mathrm{erf}\left[0.17\left(-8.5\times10^{-3}\rho_{D0}\alpha + 0.82\rho_{D0}\right)^{0.8473}\right]\right\}_{clean} \tag{67}$$

Therefore, the solar radiation absorbed by PV is corrected as follows:

$$\bar{G}_{T(\tau)} = \bar{G}_T \cdot \tau \tag{68}$$

Substituting Equation (68) into Equation (51) yields the corrected PV power model:

$$P_{PV} = Y_{PV} f_{PV}\left(\frac{\bar{G}_T\tau}{\bar{G}_{T,stc}}\right)\left[1+\varphi_P\left(T_C - T_{C,stc}\right)\right] \tag{69}$$

When the PV surface integrates a TENG (light transmittance is τ_1), the power model is further expressed as:

$$P_{PV} = Y_{PV} f_{PV}\left(\frac{\bar{G}_T\tau\tau_1}{\bar{G}_{T,stc}}\right)\left[1+\varphi_P\left(T_C - T_{C,stc}\right)\right] \tag{70}$$

It is evident that factors such as solar intensity, inclination angle, dust deposition, and TENG transmittance all influence PV performance. Note that the inclination angle should be determined by comprehensively evaluating factors such as the local solar altitude angle and dust deposition, as shown in Fig. S17.

Note S8 Mechanical energy conversion efficiency of the EMG

For the EMG, the input mechanical energy W_{in} is[R11]:

$$W_{\text{in}} = \frac{1}{4} mR^2 \left(\omega_0^2 - \omega_1^2 \right) \tag{71}$$

where m is the rotational mass, R is the radius of rotation, and ω_0 and ω_1 are the angular velocities (rad/s) before and after the load R_L is connected, respectively.

The electrical energy generated by the EMG is described as follows:

$$W_e = P_{av} \cdot t \tag{72}$$

Hence, the energy conversion efficiency η_1 can be described as follow:

$$\eta_1 = \frac{W_e}{W_{\text{in}}} = \frac{P_{av} \cdot t}{0.25 mR^2 \left(\omega_0^2 - \omega_1^2 \right)} \tag{73}$$

For the rotary EMG which working at wind speed of 10 m/s, W_e is 87.35 mJ at 6.5 kΩ. m is 62.4 g, ω_0 is 32.75π rad/s, ω_1 is 23.15π rad/s, R is 3.7 cm, W_{in} is 112.86 mJ. Hence, the energy conversion efficiency η_1 is up to 77.4%.

Note S9 Mechanical energy conversion efficiency of the TENG

For TENG, the energy conversion efficiency η_2 can be expressed as[48,50]:

$$\eta_2 = \frac{E_{out}}{E_{in}} = \int \frac{V^2}{R_L} dt / mgH \tag{74}$$

where the gravitational acceleration g= 9.8 ms^{-2}, m is the mass of droplet, and H is the drop height.

Here, m= 4.55×10^{-5} kg for the 45.5 μL droplet. Thus, the mechanical energy carried by one water droplet released from a height of 80 cm is roughly 3.57×10^{-4} J, and the generated electrical energy is calculated as 1.83×10^{-6} J. The corresponding η_2 is 5.1%.

References

[R1] Liao S, Qin S. Physical significance of artificial numerical noise in direct numerical simulation of turbulence. Journal of Fluid Mechanics, 2025, 1008: R2.

[R2] Hoste J J O, Gibbons N N, Ecker T, et al. A review of Reynolds-averaged Navier–Stokes modeling for hypersonic large cone–flares. Physics of Fluids, 2025, 37(2).

[R3] Norberg C. Fluctuating lift on a circular cylinder: review and new measurements. Journal of Fluids and Structures, 2003, 17(1): 57-96.

[R4] Jiang H, Ju X, Zhao M, et al. Large-eddy simulation of vortex-induced vibration of a circular cylinder at Reynolds number 10000. Physics of Fluids, 2024, 36(8).

[R5] Dong S, Karniadakis G E. DNS of flow past a stationary and oscillating cylinder at Re= 10000. Journal of fluids and structures, 2005, 20(4): 519-531.

[R6] Zhao L C, Zou H X, Yan G, et al. Magnetic coupling and flextensional amplification mechanisms for high-robustness ambient wind energy harvesting. Energy Conversion and Management, 2019, 201: 112166.

[R7] Maatallah T, El Alimi S, Nassrallah S B. Performance modeling and investigation of fixed, single and dual-axis tracking photovoltaic panel in Monastir city, Tunisia. Renewable and Sustainable Energy Reviews, 2011, 15(8): 4053-4066.

[R8] Reindl D T, Beckman W A, Duffie J A. Evaluation of hourly tilted surface radiation models. Solar energy, 1990, 45(1): 9-17.

[R9] Hegazy A A. Effect of dust accumulation on solar transmittance through glass covers of plate-type collectors. Renewable energy, 2001, 22(4): 525-540.

[R10] Nakayama, Yasuki. Introduction to fluid mechanics. Butterworth-Heinemann, 2018.

[R11] He W, Shan C, Fu S, et al. Large harvested energy by self-excited liquid suspension triboelectric nanogenerator with optimized charge transportation

behavior. Advanced Materials, 2023, 35(7): 2209657.